TABLE 5
Correlation of Disease Progression and Genomic Status*

	+	−	
TP53 (17p13) deletion	+	−	
Disease progression			
+	3	11	
−	0	38	P = .002
ATM (11q22) deletion	+	−	
Disease progression			
+	3	11	
−	3	35	P = .122
Additional genomic abnormalities[†]	+	−	
Disease progression			
+	6	8	
−	17	21	P = .872
ZAP-70 expression	+	−	
Disease progression			
+	7	7	
−	12	26	P < .001
IgVH status	Nonmutated	Mutated	
Disease progression			
+	9	5	
-	8	30	P < .001

+ Indicates presence; −, absence; IgVH, immunoglobulin heavy-chain.
* Correlations of disease progression and genomic abnormalities were examined by using the chi-square test. The clinical status of 51 patients was examined, and P values are shown.
† Additional abnormalities included genomic abnormalities (see Tables 2 and 3) other than the 4 common genetic abnormalities (trisomy 12, deletion of TP53, deletion of ATM, and deletion of 13q14).

TABLE 6
Correlation of Genomic Abnormalities

	+	−	
Trisomy 12	+	−	
13q14 Deletion			
+	0	33	
−	4	19	P = .010
TP53 (17q13) deletion	+	−	
Additional abnormality*			
+	3	22	
−	0	31	P = .034
13q14 Deletion	+	−	
Additional abnormality*			
+	12	14	
−	21	10	P = .046

+ Indicates presence; −, absence.
* Additional abnormalities included genomic abnormalities (see Tables 2 and 3) other than the 4 common genetic abnormalities (trisomy 12, deletion of TP53, deletion of ATM, and deletion of 13q14). P values are shown.

These higher resolution SNP-chips will have greater sensitivity to detect this small deletion in CLL comparable to the sensitivity of FISH analysis. We believe that the higher resolution (250-500 k) SNP-chip will be able to supplant FISH and cytogenetics.

One of the advantages of our method is that we can detect allele-specific gene dosage levels without matched normal controls. We used pooled data from several hundred normal DNA samples, and our computerized software selected optimal reference data for individual CLL samples.[13] This new technique allowed us precisely to detect UPD, one of the common genetic abnormalities observed in cancers, without matched control DNA.[13] It is noteworthy that we identified 2 patients with UPD of the whole chromosome 13 among patients with homozygous deletion of 13q14 (Patients 23 and 24). This finding pinpoints the usefulness of SNP-chip analysis to detect copy number neutral loss of heterozygosity. It also suggests that homozygosity of the whole chromosome 13 is a step in the clonal evolution of CLL, resulting in the loss of both alleles at the CDR on 13q14. We also observed UPD and deletions that involved 17p13, which contains the tumor suppressor gene TP53. Sequencing the TP53 gene in the sample with UPD showed a previously reported polymorphic nucleotide change at codon 72 in both alleles. It is unclear whether TP53 is the target gene of this UPD.

Recently, Pfeifer et al reported an SNP-chip analysis of 70 CLL samples using 10- to 50-k Affymetrix GeneChip genomic microarrays.[21] The difference between our study and theirs is that we examined patients with early-stage CLL who were not treated at the time the samples were collected, whereas Pfeifer et al analyzed patients in all stages of CLL, and approximately 50% of their patients previously had received chemotherapy. Chemotherapeutic reagents, especially alkylating reagents (which are used frequently to treat CLL[22]), damage DNA and lead to therapy-related genetic abnormalities.[23] Furthermore, treatments with chemotherapeutic reagents select the resistant clones in CLL, and drug-resistant clones become dominant after prolonged treatment.[24] Those clones may be different from initial CLL malignant cells. Our patients were not treated with any reagents and most likey had genetic events that occurred during the early stage of development of CLL. Although Pfeifer et al observed duplication/amplification of 2p involving Rel and BCL11A,[21] we did not observe these genetic abnormalities. Duplication/amplification of Rel and BCL11A may be associated with either advanced disease or secondary events caused by chemotherapeutic treatment.

Pfeifer et al also reported that patients who had CLL with biallelic loss of 13q14 had a worse prognosis.[21] In our study, 15 of 33 patients who had 13q14 deletion had clones with biallelic loss of this region (percentages of clones with biallelic loss, 3%-64%) detected by FISH. Only 4 of those 15 patients with biallelic loss of 13q14 (percentage of cells with biallelic loss: 8%, 11%, 28%, and 35%) developed progressive disease.

Therefore, biallelic loss of 13q14 did not appear have an adverse effect on the prognosis of patients CLL in our study ($P = .953$) (Supplementary Table).

We demonstrated that 13q14 deletion and trisomy 12 were exclusive of each other. MiR15a/16-1 commonly are deleted in patients with 13q14 deletions. MiR15a/16-1 are micro-RNAs that block the function of a variety of target genes.[25] Cyclin D2 is one of the target genes of these micro-RNAs (available at URL: http://www.targetscan.org/ Accessed on August 1, 2007) and is localized on 12p13. Overexpression of cyclin D2 is observed frequently in CLL.[26] Deletion of miR15a/16-1 may lead to restoration of cyclin D2 expression in CLL; likewise, trisomy 12 may be an alternative means to enhance expression of this gene. Cyclin D2 may be a common downstream target of both deletion of 13q14 and trisomy 12. Unfortunately, we were not able to obtain expression levels of cyclin D2 or miR15a/16-1 in our samples. Future analysis will elucidate the correlations of these important genes in the development of CLL.

In summary, the results from the current study suggest that SNP arrays can accurately detect the common abnormalities in CLL. The technique also revealed a large number of new abnormalities, especially smaller regions that were undetected by prior methods. Several of these abnormalities involve genes of potential interest, because they may be causative of CLL and will require further study. The SNP-chip is a rapid, robust assay that can survey the entire genome, provide diagnostic and prognostic clarity, and help identify new therapeutic targets. The cost of the assay is decreasing quickly, and it has the potential to replace conventional techniques.

REFERENCES

1. Zwiebel JA, Cheson BD. Chronic lymphocytic leukemia: staging and prognostic factors. *Semin Oncol.* 1998;25:42–59.
2. Seiler T, Dohner H, Stilgenbauer S. Risk stratification in chronic lymphocytic leukemia. *Semin Oncol.* 2006;33:186–194.
3. Binet JL, Caligaris-Cappio F, Catovsky D, et al. Perspectives on the use of new diagnostic tools in the treatment of chronic lymphocytic leukemia. *Blood.* 2006;107:859–861.
4. Oscier D, Fegan C, Hillmen P, et al. Guidelines on the diagnosis and management of chronic lymphocytic leukaemia. *Br J Haematol.* 2004;125:294–317.
5. Shanafelt TD, Geyer SM, Kay NE. Prognosis at diagnosis: integrating molecular biologic insights into clinical practice for patients with CLL. *Blood.* 2004;103:1202–1210.
6. Dohner H, Stilgenbauer S, Benner A, et al. Genomic aberrations and survival in chronic lymphocytic leukemia. *N Engl J Med.* 2000;343:1910–1916.
7. Migliazza A, Bosch F, Komatsu H, et al. Nucleotide sequence, transcription map, and mutation analysis of the 13q14 chromosomal region deleted in B-cell chronic lymphocytic leukemia. *Blood.* 2001;97:2098–2104.
8. Bullrich F, Fujii H, Calin G, et al. Characterization of the 13q14 tumor suppressor locus in CLL: identification of ALT1, an alternative splice variant of the LEU2 gene. *Cancer Res.* 2001;61:6640–6648.
9. Calin GA, Dumitru CD, Shimizu M, et al. Frequent deletions and down-regulation of micro-RNA genes miR15 and miR16 at 13q14 in chronic lymphocytic leukemia. *Proc Natl Acad Sci USA.* 2002;99:15524–15529.
10. Calin GA, Ferracin M, Cimmino A, et al. MicroRNA signature associated with prognosis and progression in chronic lymphocytic leukemia. *N Engl J Med.* 2005;353:1793–1801.
11. Lindblad-Toh K, Tanenbaum DM, Daly MJ, et al. Loss-ofheterozygosity analysis of small-cell lung carcinomas using single-nucleotide polymorphism arrays. *Nat Biotechnol.* 2000;18:1001–1005.
12. Nannya Y, Sanada M, Nakazaki K, et al. A robust algorithm for copy number detection using high-density oligonucleotide single nucleotide polymorphism genotyping arrays. *Cancer Res.* 2005;65:6071–6079.
13. Yamamoto G, Nannya Y, Kato M, et al. Highly sensitive method for genome-wide detection of allelic composition in non-paired, primary tumor specimens using SNP genotyping microarrays. *Am J Hum Genet.* 2007;81:114–126.
14. Matutes E, Owusu-Ankomah K, Morilla R, et al. The immunological profile of B-cell disorders and proposal of a scoring system for the diagnosis of CLL. *Leukemia.* 1994;8:1640–1645.
15. Sambrook J, Russell DW. Molecular Cloning: A Laboratory Manual. 3rd ed. Cold Spring Harbor, NY: Cold Spring Harbor Laboratory Press; 2001.
16. Crespo M, Bosch F, Villamor N, et al. ZAP-70 expression as a surrogate for immunoglobulin-variable-region mutations in chronic lymphocytic leukemia. *N Engl J Med.* 2003;348:1764–1775.
17. Xiong Z, Laird PW. COBRA: a sensitive and quantitative DNA methylation assay. *Nucleic Acids Res.* 1997;25:2532–2534.
18. Kalachikov S, Migliazza A, Cayanis E, et al. Cloning and gene mapping of the chromosome 13q14 region deleted in chronic lymphocytic leukemia. *Genomics.* 1997;42:369–377.
19. Largaespada DA. Haploinsufficiency for tumor suppression: the hazards of being single and living a long time. *J Exp Med.* 2001;193:F15–F18.
20. Stankovic T, Weber P, Stewart G, et al. Inactivation of ataxia telangiectasia mutated gene in B-cell chronic lymphocytic leukaemia. *Lancet.* 1999;353:26–29.
21. Pfeifer D, Pantic M, Skatulla I, et al. Genome-wide analysis of DNA copy number changes and LOH in CLL using high-density SNP arrays. *Blood.* 2007;109:1202–1210.
22. Robak T, Kasznicki M. Alkylating agents and nucleoside analogues in the treatment of B cell chronic lymphocytic leukemia. *Leukemia.* 2002;16:1015–1027.
23. Karp JE, Smith MA. The molecular pathogenesis of treatment-induced (secondary) leukemias: foundations for treatment and prevention. *Semin Oncol.* 1997;24:103–113.
24. Bosanquet AG, Bell PB. Novel ex vivo analysis of nonclassical, pleiotropic drug resistance and collateral sensitivity induced by therapy provides a rationale for treatment strategies in chronic lymphocytic leukemia. *Blood.* 1996;87:1962–1971.
25. Yoon S, De Micheli G. Prediction of regulatory modules comprising microRNAs and target genes. *Bioinformatics.* 2005;21(suppl 2):ii93–ii100.
26. Delmer A, Ajchenbaum-Cymbalista F, Tang R, et al. Overexpression of cyclin D2 in chronic B-cell malignancies. *Blood.* 1995;85:2870–2876.

Dehydroxymethylepoxyquinomicin (DHMEQ) therapy reduces tumor formation in mice inoculated with Tax-deficient adult T-cell leukemia-derived cell lines

Takeo Ohsugi [a,*], Toshio Kumasaka [b], Seiji Okada [c], Takaomi Ishida [d], Kazunari Yamaguchi [e], Ryouichi Horie [f], Toshiki Watanabe [d], Kazuo Umezawa [g]

[a] Division of Microbiology and Genetics, Center for Animal Resources and Development, Institute of Resource Development and Analysis, Kumamoto University, 2-2-1 Honjo, Kumamoto 860-0811, Japan

[b] Department of Human Pathology, Juntendo University Graduate School of Medicine, 2-1-1 Hongo, Bunkyo-ku, Tokyo 113-8421, Japan

[c] Division of Hematopoiesis, Center for AIDS Research, Kumamoto University, 2-2-1 Honjo, Kumamoto 860-0811, Japan

[d] Laboratory of Tumor Cell Biology, Department of Medical Genome Sciences, Graduate School of Frontier Sciences, The University of Tokyo, 4-6-1 Shirokanedai, Minato-ku, Tokyo 108-8639, Japan

[e] Department of Safety Research on Blood and Biologics, National Institute of Infectious Diseases, Gakuen 4-7-1, Musashimurayama-shi, Tokyo 208-0011, Japan

[f] Department of Hematology, Faculty of Medicine, Kitasato University, 1-15-1 Sagamihara, Kanagawa 228-8555, Japan

[g] Department of Applied Chemistry, Faculty of Science and Technology, Keio University, 3-14-1 Hiyoshi, Kohoku-ku, Yokohama 223-0061, Japan

Abstract

Adult T-cell leukemia (ATL) is an aggressive neoplasm caused by human T-cell leukemia virus type I (HTLV-I), which induces nuclear factor-κB (NF-κB), a molecule central to the ensuing neoplasia. The NF-κB inhibitor dehydroxymethylepoxyquinomicin (DHMEQ) has been shown to inhibit NF-κB activation in Tax-expressing HTLV-I-infected cells. In this study, we used NOD/SCID β2-microglobulin^{null} mice to show that intraperitoneal inoculation with Tax-deficient ATL cell lines caused rapid death, whereas DHMEQ-treated mice survived. Furthermore, DHMEQ treatment after subcutaneous inoculation inhibited the growth of transplanted ATL cells. These results demonstrate that DHMEQ has therapeutic efficacy on ATL cells, regardless of Tax expression.
© 2007 Elsevier Ireland Ltd. All rights reserved.

Keywords: HTLV-I; ATL; DHMEQ; NF-κB; NOD/SCID β2-microglobulin^{null} mice

1. Introduction

Adult T-cell leukemia (ATL) is a mature T-cell malignancy caused by human T-cell leukemia virus type I (HTLV-I) infection [1,2]. A minor proportion of HTLV-I-infected carriers develop ATL after a long latency period. However, almost 1000 cases of ATL are diagnosed each year in Japan, no accepted curative therapy for ATL exists, and patients progress to death with a mean survival time of 13 months [3]. ATL patients retain poor prognosis mainly because of resistance to conventional, high-dose, or combination chemotherapy treatment [4]. Therefore, development of novel anti-ATL therapies is greatly needed.

Tax, a 40 kDa protein encoded by the pX region of HTLV-I viral genome activates nuclear factor-κB (NF-κB) by stimulating the activity of the IκB kinase (IKK), which in turn leads to phosphorylation and degradation of IκBα [5,6]. NF-κB is then released from IκBα and translocates to the nucleus where it transactivates various genes encoding cytokines, chemokines and anti-apoptotic proteins [7]. However, NF-κB also may be activated in primary ATL cells and some ATL-derived cell lines that lack viral expression [7–9]. These facts show that Tax-independent mechanisms for constitutive NF-κB activation are present in ATL cells. Regardless of Tax expression, constitutive activation of NF-κB in ATL cells is required for ATL cell growth and survival [7]. Thus, blocking the NF-κB pathway may be a key strategy for the treatment of ATL patients [10,11].

The NF-κB inhibitor, dehydroxymethylepoxyquinomicin (DHMEQ), inhibits activation of NF-κB by preventing nuclear translocation of p65, an NF-κB subunit [12–14]. DHMEQ has already shown potential for inducing apoptosis in prostate cancer, thyroid cancer, pancreatic cancer, multiple myeloma and breast cancer [15–20]. We recently reported that DHMEQ strongly inhibits constitutively activated NF-κB in both ATL-derived cell lines and in primary cultures of ATL cells from patients, inducing apoptosis in these cells at concentrations that do not affect the viability of peripheral blood mononuclear cells [9]. We also observed that DHMEQ induces apoptosis in the Tax-expressing HTLV-I-infected cell lines MT-2 and HUT-102 and inhibits nuclear translocation of the p65 subunit in vitro and in vivo [21,22]. However, we could not evaluate the effects of DHMEQ on the Tax-deficient ATL-derived cell lines TL-Om1 and MT-1 in vivo,

because these cells did not grow in severe combined immunodeficiency (SCID) mice in which natural killer (NK) cell activity had been eliminated (NK-free SCID mice) [21].

In this study, we establish a mouse model of ATL using non-obese diabetic (NOD)/SCID and β2-microglobulin knockout (NOD/SCID β2m^{null}) mice that have low NK cell activity and additionally lack β2-microglobulin (β2m), the light chain of the MHC class I molecule [23]. We inoculated these mice intraperitoneally or subcutaneously with either TL-Om1 or MT-1 and evaluated the effect of DHMEQ treatment in vivo. Mice injected with TL-Om1 or MT-1 cells intraperitoneally but not treated with DHMEQ died soon thereafter from tumor and infiltrative leukemic cell growth, whereas DHMEQ-treated mice survived and showed a decreased rate of inoculated cell infiltration. In the subcutaneous model, DHMEQ induced apoptosis and inhibited the growth of TL-Om1 cells transplanted at the injection site.

2. Materials and methods

2.1. Cell lines

Four HTLV-I-infected T-cell lines, TL-Om1 [24], MT-1 [2], MT-2 [25] and HUT-102 [1], were maintained at 37 °C in 5% CO_2 in RPMI 1640 medium supplemented with 10% fetal bovine serum, 100 U/ml of penicillin and 100 μg/ml of streptomycin. TL-Om1 and MT-1 are leukemic T-cell lines derived from patients with ATL. MT-2 is an HTLV-I-transformed T-cell line established by an in vitro co-culture protocol. HUT-102 was established from a patient originally diagnosed with cutaneous T-cell lymphoma which was later considered a lymphoma type ATL. The clonal origin of this cell line is unclear, and can no longer be determined. An HTLV-I-negative T-cell line, MOLT-4, was maintained in RPMI 1640 supplemented with 10% fetal bovine serum at 37 °C in 5% CO_2 and the antibiotics listed above. All cells lines were passaged twice a week.

2.2. Characterization of HTLV-I-infected cell lines

To analyze cell cultures for the presence of Tax mRNA, total RNA from cells was extracted using an RNA extraction kit (Qiagen, Valencia, CA) and treated with 10 U DNase I (Takara Bio, Tokyo, Japan) for 30 min at 37 °C. Reverse transcriptase polymerase chain reaction (RT-PCR) was performed using a one-step RNA PCR kit (Takara Bio) with a set of primers for the Tax mRNA [26].

To analyze cell cultures for the presence of Tax protein, samples containing 50 μg of total protein from cell lysates were electrophoresed and transferred to a polyvinylidene difluoride membrane (Atto, Tokyo, Japan). Western blot analysis was carried out to detect Tax protein in each cell line as described [22].

To evaluate viral release into the supernatant, culture samples were taken 3 days after passage. Cell culture medium was centrifuged at 1200g for 10 min at 4 °C. Supernatants were then examined for the presence of the HTLV-I p19 antigen using an enzyme-linked immunosorbent assay (ELISA) according to the manufacturer's protocol (Zeptomatrix, Buffalo, NY).

For evaluation of NF-κB activity, the cells (5 × 10^6) were centrifuged at 200g for 5 min at 4 °C and washed with cold phosphate-buffered saline and nuclear extracts were subsequently prepared using a nuclear extraction kit (Active Motif, Carlsbad, CA). DNA-binding activity of NF-κB p65 was then measured using microplate-based ELISAs according to the manufacturer's protocol (Trans-AM NF-κB p65 Transcription Factor Assay kit; Active Motif). Absorbance at 450 nm was determined in each well using a microplate reader (Bio-Rad, Richmond, CA).

2.3. Chemicals

Racemic DHMEQ was synthesized as described [13], dissolved in DMSO and subsequently diluted in culture medium to a final concentration of <0.1%.

2.4. Nuclear staining to determine apoptosis in vitro

Cells (1 × 10^6) were cultured with 20 or 40 μg/ml of DHMEQ for 48 h. Cells treated with the same concentrations of DMSO solvent without DHMEQ served as controls. Morphologic examination of cells was performed using a phase contrast microscope (CK40: Olympus, Tokyo, Japan). Cells were stained with Hoechst 33342 (Calbiochem, San Diego, CA) and stained apoptotic nuclei were calculated as reported [21,22].

2.5. Measurement of NF-κB activity in cells treated with DHMEQ

TL-Om1 or MT-1 cells (5 × 10^6) were cultured with 20 or 40 μg/ml DHMEQ for 16 h. The HTLV-I-uninfected T-cell line, MOLT-4, served as a control. Nuclear and cytoplasmic fractions were then prepared using a nuclear extraction kit according to the manufacturer's protocol (Active Motif). NF-κB activity in nuclear and cytoplasmic fractions was determined by measuring the DNA-binding activity of p65, as described above, and was expressed as a percentage of the binding measured in control cells that were not treated with DHMEQ. The relative ratio of nuclear to cytoplasmic p65 was calculated from the absorbance value of nucleus divided by that of cytoplasm.

2.6. Mice

Non-obese diabetic (NOD)/severe combined immunodeficiency (SCID) and β2-microglobulin knockout (NOD/SCID β2m^{null}) mice were obtained from The Jackson Laboratory (Bar Harbor, ME). The mice were maintained under specific pathogen-free conditions in laminar-flow benches at 22 ± 2 °C with a 12 h light/dark cycle. Mice were fed sterilized (γ-irradiated) pellets and received acidified drinking water (pH 2.5–3.0) ad libitum. All procedures involving animals and their care were approved by the animal care committee of Kumamoto University in accordance with Institutional and Japanese government guidelines for animal experiments.

2.7. Administration of DHMEQ to NOD/SCID β2m^{null} mice injected intraperitoneally with TL-Om1 or MT-1 cells

TL-Om1 or MT-1 cells (5 × 10^7) were washed three times with phosphate-buffered saline and introduced by intraperitoneal injection into 7- to 10-week-old NOD/SCID β2m^{null} mice that had been pretreated 1 day earlier with 2 Gy irradiation. DHMEQ was dissolved in 0.5% carboxymethyl cellulose (vehicle) to a final concentration of 1.2 mg/ml. DHMEQ (12 mg/kg) or vehicle was administered intraperitoneally on day 0 of cell inoculation and three times a week thereafter for 5 weeks. Mice surviving for 5 weeks after cell inoculation were autopsied and tumor formation was assessed.

2.8. Histology

Organs were fixed in 10% neutral-buffered formalin immediately after removal, embedded in paraffin, cut into 4 μm sections, and stained with hematoxylin and eosin.

2.9. PCR analysis of genomic DNA

To detect HTLV-I proviral sequences, 0.5 μg of genomic DNA extracted from tumors or various organs was subjected to PCR analysis [21,22]. Oligonucleotide primers for tax and for the human β-globin genes (control) were used and PCR was performed as described [21,22].

2.10. Administration of DHMEQ to NOD/SCID β2m^{null} mice injected with TL-Om1 subcutaneously

DHMEQ was dissolved in 0.5% carboxymethyl cellulose (vehicle) to a final concentration of 1.2 mg/ml. TL-Om1 cells (5 × 10^7) were washed three times with phosphate-buffered saline and introduced by subcutaneous injection into the post-auricular region of 7- to 10-week-old NOD/SCID β2m^{null} mice that had been pretreated 1 day earlier with 2 Gy irradiation. DHMEQ

(12 mg/kg) or vehicle was administered by intraperitoneal injection on day 0 of cell inoculation and three times a week thereafter for 5 weeks. Both tumor size and body weight were measured weekly. Tumor volume was calculated according to the formula: $a^2 \times b \times 0.5$, where a and b are the smallest and largest diameters, respectively.

2.11. Detection of apoptosis in vivo

Animals were sacrificed 5 weeks after cell inoculation. Gross tumors were immediately fixed in 10% neutral-buffered formalin, appropriately cut and then embedded in paraffin. The tissues were sectioned to 4 μm thickness and stained with hematoxylin and eosin. Apoptosis in tissue sections was examined by TUNEL (terminal deoxynucleotidyl transferase-mediated deoxyuridine triphosphate nick end-labeling) assay using the *in situ* Apoptosis Detection kit (R&D systems, Minneapolis, MN) according to the manufacturer's instructions.

2.12. Statistical analysis

Statistical analysis was performed using Fisher's exact probability test and Student's *t*-test. Statistical significance was defined as $P < 0.05$.

3. Results

3.1. Characterization of HTLV-I-associated cell lines

As expected, MT-2 and HUT-102 expressed significant amounts of Tax mRNA and protein (Fig. 1a). MT-1 cells expressed the HTLV-I Tax transcript, but we were unable to detect Tax protein (Fig. 1a, lower panel). TL-Om1 cells did not express detectable amounts of Tax at either mRNA or protein levels. To assess virus release in these cell lines, we analyzed for the presence of HTLV-I Gag protein in cell culture supernatants using a p19-specific ELISA. MT-2 and HUT-102 cells expressed high levels of the HTLV-I Gag protein, p19, whereas only small amounts of p19 (10^4- to 10^5-fold lower than that of MT-2 and HUT-102) were detected in the ATL-derived cell lines TL-Om1 and MT-1 (Fig. 1a, upper panel). The HTLV-I-uninfected human T-cell line MOLT-4 did not express p19 Gag protein (data not shown).

Next, the activity of NF-κB in these cell lines was determined by ELISA. All of these cells showed constitutive NF-κB activity, which was elevated compared with MOLT-4 cells (Fig. 1b). TL-Om1 cells showed the highest mean levels of NF-κB activity among the tested cell lines, although they did not express Tax or viral antigens. There was no significant difference in NF-κB activity between Tax-expressing and non-expressing HTLV-I-associated cell lines, as described [27].

3.2. DHMEQ inhibits NF-κB in Tax-deficient HTLV-I-associated cell lines

We evaluated the effects of DHMEQ on two HTLV-I-associated cell lines that lack Tax protein (TL-Om1 and MT-1). Morphologically, DHMEQ induced significant apoptosis as shown by deletion of cell clusters and nuclear fragmentation (Fig. 1c). After 48 h of DHMEQ treatment, Hoechst 33342 staining of nuclei showed significant apoptosis in both TL-Om1 and MT-1 cell lines (Fig. 1d). We next examined the effects of DHMEQ on the constitutive DNA binding activity of NF-κB in these cells. The cells were cultured with various concentrations of DHMEQ (0, 20 or 40 μg/ml) for 16 h (Fig. 1e). Both concentrations of DHMEQ inhibited NF-κB activation in MT-1 cells by approximately 60% compared to control cells. Likewise, DHMEQ (20 and 40 μg/ml) inhibited NF-κB activation in TL-Om1 cells by approximately 80% and 90%, respectively, compared to control cells. NF-κB p65 translocation to the nucleus was inhibited in TL-Om1 and MT-1 cells treated with DHMEQ (Fig. 1f). The relative nuclear-to-cytoplasmic ratio of p65 in TL-Om1 and MT-1 cells without DHMEQ was >3.0 and 1.5, respectively, whereas in cells treated with DHMEQ, the ratio was the same as in the HTLV-I-uninfected T-cell line, MOLT-4. These results are consisted with our previous report [9].

3.3. DHMEQ inhibits death in mice inoculated intraperitoneally with Tax-deficient HTLV-I-infected cell lines

To evaluate the anti-tumor effect of DHMEQ against HTLV-I-infected cell lines derived from ATL patients, intraperitoneal inoculation of NOD/SCID β2m^{null} mice with 5×10^7 TL-Om1 or MT-1 cells was performed. A dose of 12 mg/kg of either DHMEQ or vehicle was administrated via intraperitoneal injection on day 0 of cell inoculation and three times a week thereafter for 5 weeks. Whereas 5 of 6 (83%) DHMEQ-treated mice were alive 5 weeks after TL-Om1 inoculation, all 6 of the control (vehicle-treated) mice died by 4 weeks after cell inoculation ($P = 0.008$ by Fisher's exact test; Fig. 2a). Likewise, only 1 of 5 (20%) control mice inoculated with MT-1 survived for 5 weeks after cell inoculation, whereas all 6 of the DHMEQ-treated mice were alive at 5 weeks post-inoculation ($P = 0.015$ by Fisher's exact test; Fig. 2b).

In TL-Om1-inoculated mice, all of the six mice that received vehicle alone had visible tumors (see representative mouse Fig. 3a, left panel and Fig. 3b), whereas only two of six DHMEQ-treated mice (33%) formed small gross tumors ($P = 0.03$ by Fisher's exact test; see representative tumor-free mouse Fig. 3a, right panel and Fig. 3b). In MT-1-inoculated mice, 40% of mice treated with vehicle alone had gross tumors, whereas none of the mice treated with DHMEQ had gross tumors (Fig. 3b). To determine
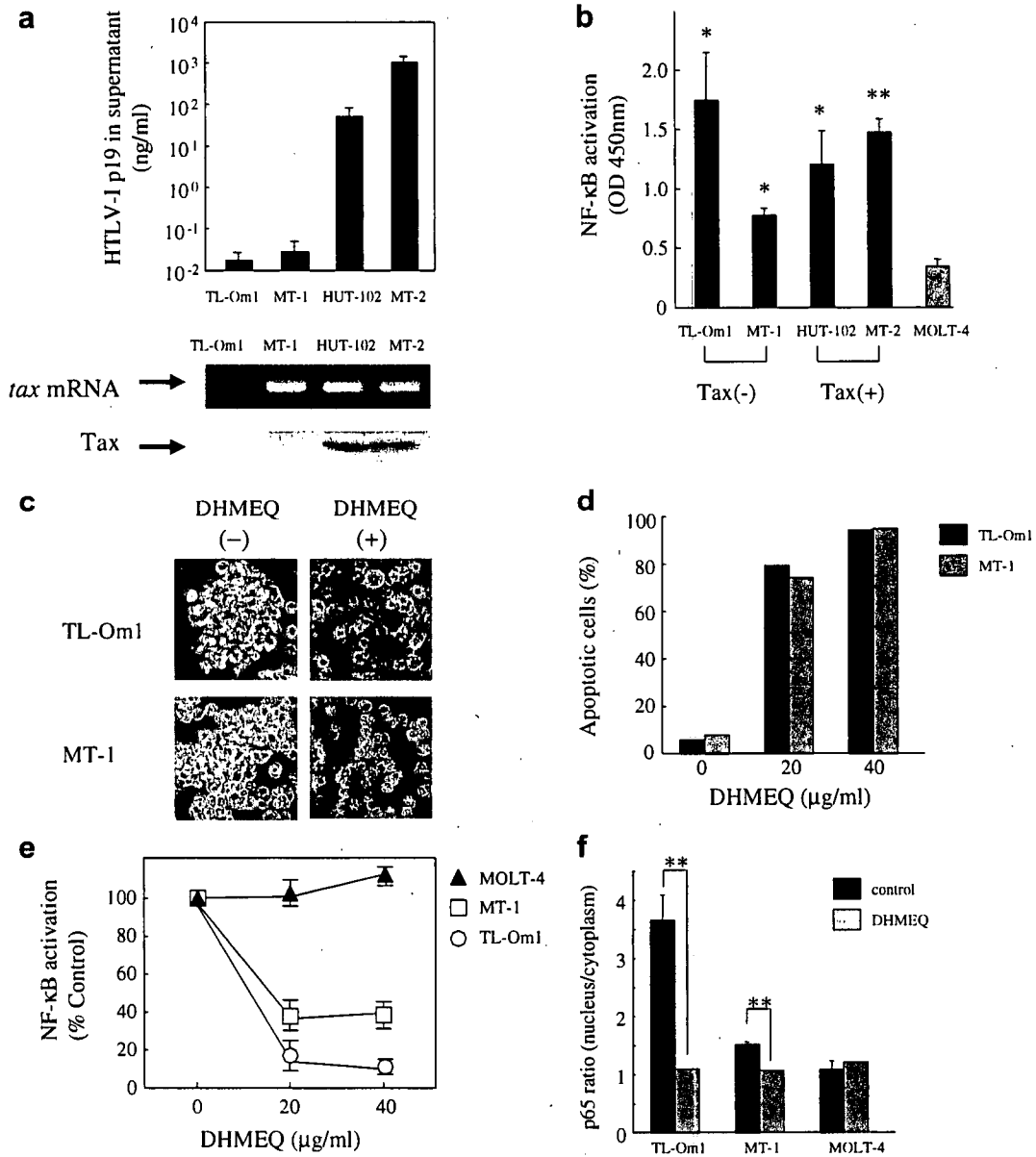
Fig. 1. Characterization of HTLV-I-associated cell lines and analysis of the effects of DHMEQ on NF-κB activity in Tax-deficient cell lines in vitro. (a) The upper panel reflects p19 Gag antigen content in culture supernatants from each cell line, as detected by ELISA. Bars represent mean values ± standard deviation (SD) of triplicate samples. The middle panel reflects Tax mRNA expression in each cell line detected by RT-PCR and the lower panel reflects Tax protein expression in each cell line detected by Western blot analysis. (b) NF-κB activity in TL-Om1, MT-1, HUT-102, MT-2 and in an uninfected cell line, MOLT-4, was measured by ELISA. This experiment was repeated three times ($n = 3$), and the data presented represent means ± SD. Statistical analysis was performed using the Student's t-test. $^*P < 0.05$, $^{**}P < 0.01$ vs. MOLT-4. (c) Morphologic examination of TL-Om1 and MT-1 cells after treatment with DHMEQ using a phase contrast microscope. TL-Om1 and MT-1 cells were treated with DHMEQ (20 μg/ml) for 24 h prior to analysis (magnification, 200×). (D) Induction of apoptosis of TL-Om1 and MT-1 cells by DHMEQ. After 48 h of DHMEQ treatment, cells were fixed and stained with Hoechst 33342. At least 1000 stained cells were counted and assessed as apoptotic or non-apoptotic. Representative results of three independent experiments are shown. (e) DHMEQ inhibits NF-κB activity in TL-Om1 and MT-1 cells. After 16 h of incubation with DHMEQ or with vehicle alone (DMSO), NF-κB activity was measured in using ELISA. MOLT-4 was used as an HTLV-I-uninfected cell control. Data are expressed as a percentage of control (vehicle-treated) activity and represent means ± SD. (f) The nuclear to cytoplasmic p65 in DHMEQ-treated cells. The results of three independent experiments are shown. Data are expressed as a percentage of control (vehicle-treated) activity and represent means ± SD. Statistical analysis was performed using the Student's t-test. $^{**}P < 0.01$ vs. control.
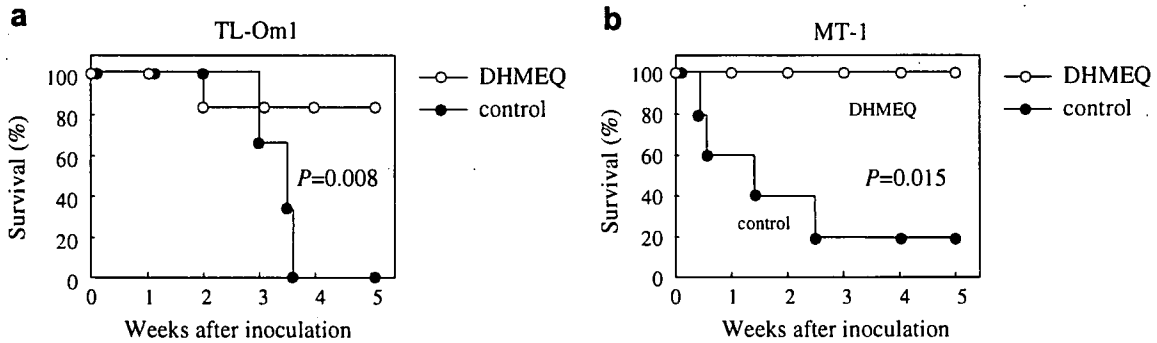
Fig. 2. DHMEQ increases survival of NOD/SCID $\beta 2m^{null}$ mice inoculated intraperitoneally with Tax-deficient HTLV-I-infected cell lines. Survival curves of mice injected with TL-Om1 cells (a) or MT-1 cells (b) in the presence of DHMEQ (12 mg/kg body weight) or carboxymethyl cellulose vehicle control. The percent of DHMEQ-treated mice that survived TL-Om1 or MT-1 inoculation was statistically different from that of the vehicle-treated control group. P, Fisher's exact test P-value.

whether the tumors were derived from inoculated cells, genomic DNA extracted from tumors was subjected to PCR using primers specific for the HTLV-I *tax* and human β-globin genes. PCR analysis showed that tumors originated from the inoculated cells (Fig. 3c).

We next compared the infiltration of inoculated cells into organs of control mice and DHMEQ-treated mice. To detect infiltration of inoculated cells into various organs, genomic DNA extracted from each organ was

subjected to PCR analysis. The organs in which both HTLV-I *tax* and human β-globin genes were detected were considered positive (Fig. 4a). In TL-Om1 inoculated mice, injected cells were present in all organ types tested from both DHMEQ-treated and untreated mice. However, the incidence of organs positive for both genes in DHMEQ-treated mice was lower than that in untreated mice. Specifically, 33% of kidneys from mice treated with DHMEQ were positive, compared with
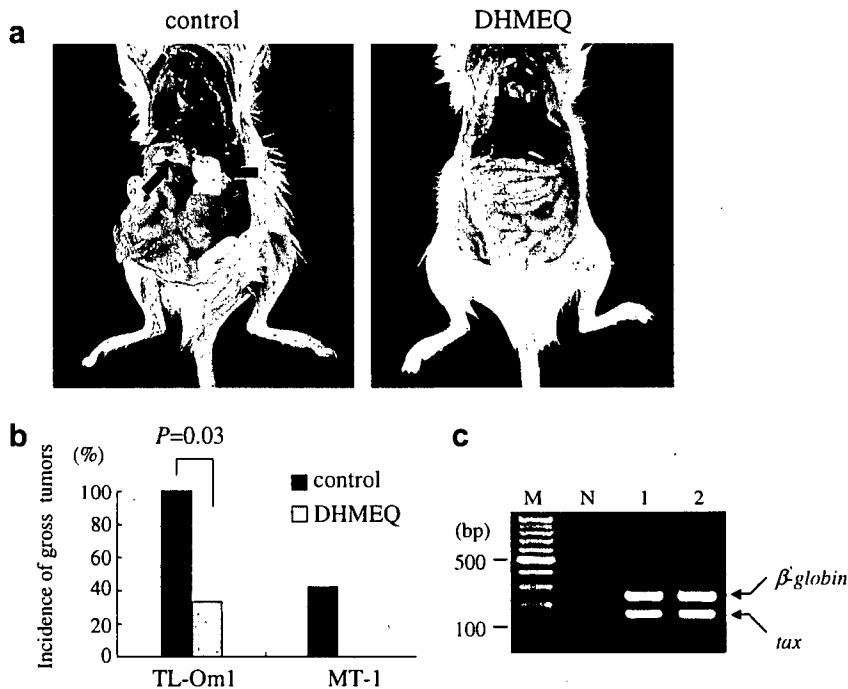

Fig. 3. DHMEQ inhibits tumor formation arising from intraperitoneal inoculation of TL-Om1 or MT-1 cells in NOD/SCID $\beta 2m^{null}$ mice. (a) In TL-Om1 inoculated mice, we observed gross tumor formation in the peritoneal cavity of vehicle-treated control mice (left) but not in DHMEQ treated mice (right). (b) DHMEQ reduces the incidence of gross tumors in mice inoculated with TL-Om1 or MT-1 cells. P, Fisher's exact test P-value. (c) PCR analysis to detect HTLV-I *tax* (159 bp PCR product) and human β-globin (262 bp PCR product) was used to determine whether tumors originated from the inoculated cells. Lane 1, tumor from TL-Om1 inoculated vehicle-treated mice; lane 2, tumor from MT-1 inoculated vehicle-treated mice; N, no template DNA; M, 100 bp ladder marker.
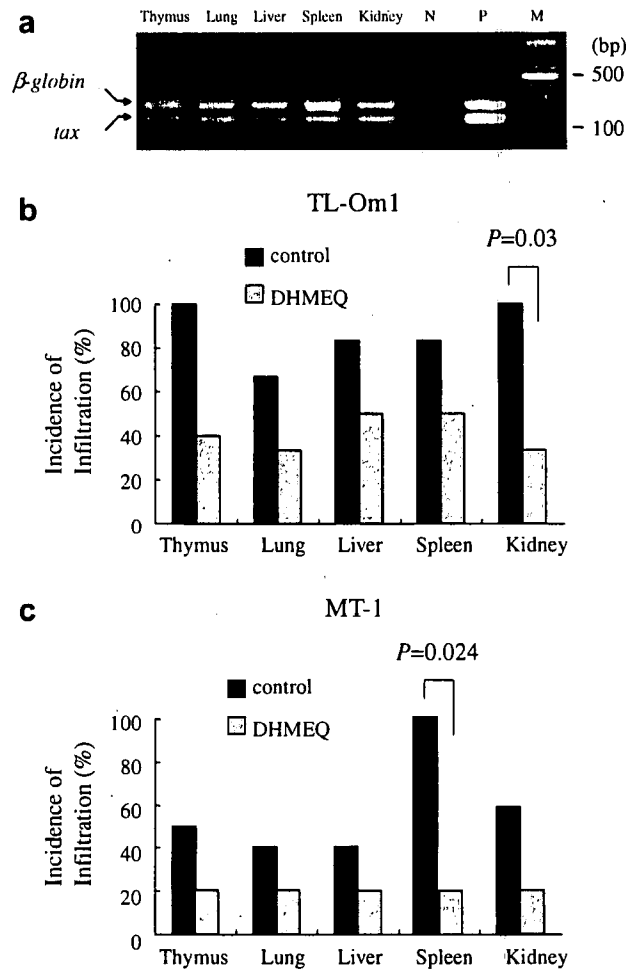
Fig. 4. PCR analysis of genomic DNA from various organs to determine infiltration of TL-Om-1 or MT-1 cells introduced by intraperitoneal inoculation in NOD/SCID β2m ^{null} mice treated with DHMEQ or vehicle (control). PCR primers were specific for either HTLV-I *tax* or human β-globin. Only those organs in which both genes were detected were considered positive. (a) Agarose gel electrophoresis of PCR reactions from a representative vehicle-treated mouse inoculated with TL-Om1 cells showing that all tested organs were positive for both genes. N, no template DNA; P, positive control from TL-Om1 cell genomic DNA; M, 100 bp ladder marker. (b and c) Graphical representation of PCR analyses indicating the infiltration of tumor cells into various organs in mice inoculated with TL-Om1 (b) or MT-1 (c) cells treated with DHMEQ or vehicle (control). P, Fisher's exact test P-value.

100% of kidneys from mice treated with vehicle alone ($P = 0.03$ by Fisher's exact test, $n = 6$ for each group; Fig. 4b).

Similarly, in MT-1 inoculated animals, the incidence of infiltrated organs in DHMEQ-treated mice was lower than that in untreated controls, although the infiltration of MT-1 cells in various organs overall was lower than that of TL-Om1 cells (Fig. 4c). Spleen infiltration was found in 20% of mice treated with DHMEQ and in 100% of mice treated with vehicle alone ($P = 0.024$ by Fisher's exact test, $n = 5$ for each group; Fig. 4c). Taken together, these data suggest that DHMEQ inhibits tumor-related death, tumor formation, and infiltration of HTLV-I-infected cells derived from ATL patients in this mouse model.

3.4. In vivo treatment of subcutaneous TL-Om1 tumors with DHMEQ

We next attempted to quantitate the effect of DHMEQ on tumors from NOD/SCID β2m^{null} mice in which TL-Om1 cells were introduced into the post-auricular area by subcutaneous injection. In control mice, tumors appeared 3 weeks after inoculation, and after 5 weeks they encompassed the whole area surrounding the cervical vertebrae (Fig. 5A; right). In contrast, mice treated with intraperitoneal DHMEQ injections had small tumors near the cervical vertebrae (Fig. 5A; left). Treatment with DHMEQ significantly inhibited the growth of TL-Om1 cells in vivo ($P < 0.05$ by Student's t-test, $n = 8$ for each

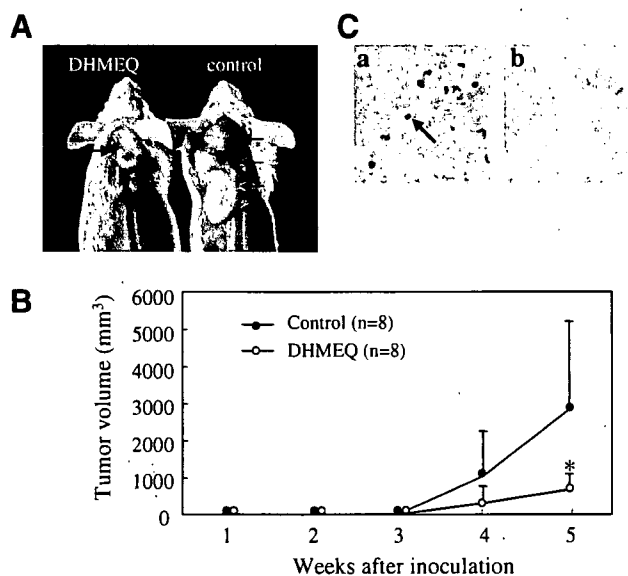**A** **C**

B

Weeks after inoculation

Fig. 5. DHMEQ inhibits tumor formation arising from subcutaneous inoculation of TL-Om1 in NOD/SCID $\beta 2m^{null}$ mice and increases apoptotic tumor cell death. TL-Om1 cells (5×10^7 per mouse) were inoculated subcutaneously in the post-auricular region. Mice were treated with intraperitoneal injections of DHMEQ (12 mg/kg) or vehicle. (A) Photograph of a representative DHMEQ-treated mouse (left) and a vehicle-treated mouse (right). (B) Serial changes in tumor volume in DHMEQ- and vehicle-treated mice. Data represent means ± SD. $^*P < 0.05$ vs. control by Student's t-test. (C) Representative TUNEL assay showing apoptosis in gross tumors from a mouse treated with DHMEQ (a). No apoptotic cells were seen in vehicle-treated tumors (b). Original magnification, 50×.

group), and the serial changes in subcutaneous tumor volume in DHMEQ-treated and untreated mice are shown in Fig. 5B. We confirmed the inoculated cell origin of all tumors recovered from the mice using PCR primers for HTLV-I *tax* and human *β-globin* genes (data not shown). To examine the effect of DHMEQ on the induction of apoptosis in these tumors, we performed TUNEL assays on tumor tissue sections. We observed no apoptotic cells in tumors from untreated mice (Fig. 5C, panel b), whereas apoptotic cells in tumors from DHMEQ-treated mice were observed (Fig. 5C, panel a).

4. Discussion

Here, we have shown that Tax expression could not be detected in MT-1 cells by Western blotting, but could be detected by RT-PCR, whereas Tax expression in TL-Om1 cells was not detected by either method. These data indicate that MT-1 and TL-Om1 cell lines do in fact closely reflect the status of Tax expression found in primary leukemic cells isolated from ATL patients [28,29]. Among the cells lines tested, NF-κB activity and the nuclear translocation of p65 were the highest in TL-Om1 cells. In both TL-Om1 and MT-1 cells, DHMEQ induced apoptosis and inhibited activation of NF-κB by reducing the nuclear translocation of p65 to levels

found in the HTLV-I-uninfected cell line MOLT-4. These results suggest that Tax-independent mechanisms for induction of NF-κB activation exist in these cells, and that DHMEQ inhibits both Tax-dependent and -independent mechanisms of NF-κB activity in ATL cells. In agreement with this, NF-κB inhibition by DHMEQ has been shown to down-regulate expression of genes involved in anti-apoptosis or cell cycle progression [9].

To establish the growth of the ATL-derived cell lines TL-Om1 and MT-1 in mice, we used NOD/SCID $\beta 2m^{null}$ mice – which have low NK cell activity and lack β2-microglobulin (β2 m) [23]. Mice inoculated with these cells via intraperitoneal injection showed rapid death from tumors. We demonstrated that DHMEQ also inhibited tumor formation, inhibited infiltration of inoculated cells into various organs, and reduced mortality in NOD/SCID $\beta 2m^{null}$ mice inoculated with Tax-deficient ATL-derived cell lines. It is important to note that these data resemble the effects of DHMEQ in NK-free SCID mice injected with the Tax-expressing HTLV-I-transformed cell lines MT-2 and HUT-102 [21,22] and suggest that DHMEQ may have broad application for treatment of ATL patients. We found that 100% of NOD/SCID $\beta 2m^{null}$ mice inoculated with TL-Om1 cells formed

gross tumors (defined as having a largest measured diameter of >3 mm) in the peritoneal cavity, whereas only 40% of MT-1-inoculated animals demonstrated gross tumor formation. In fact, control mice that were injected with MT-1 primarily formed very small disseminated masses, rather than gross tumors, within the peritoneal cavity. However, the origin of these masses could not be identified because we could not detect either the HTLV-I *tax* or human *β-globin* genes by PCR due to the small amount of genomic DNA available.

The TL-Om1 cell line was chosen for further analysis of the anti-tumor effects of DHMEQ because 100% of TL-Om1-inoculated NOD/SCID $\beta 2m^{null}$ mice formed gross tumors in the peritoneal cavity. We showed that DHMEQ suppressed the growth of transplanted cells in NOD/SCID $\beta 2m^{null}$ mice injected with TL-Om1 cells subcutaneously, in contrast to the significant increase in tumor burden observed in non-treated mice. Furthermore, apoptotic cells were present in tumors from DHMEQ-treated mice, similar to that reported for Tax-expressing HTLV-I-transformed cells [21]. Although mice injected subcutaneously with HUT-102 cells have been shown to form tumors at the inoculation site and have shown infiltration of inoculated cells into various organs [22], we could not detect the infiltration of TL-Om1 cells into other organs in either DHMEQ-treated or non-treated mice inoculated with TL-Om1 cells subcutaneously. This discrepancy is probably due to tumor volume at the inoculation site, because we found little difference in infiltration of these cells via intraperitoneal injection in each mouse model [21]. However, this system was useful for directly measuring response to DHMEQ in vivo and for detecting apoptosis.

In conclusion, DHMEQ significantly prevented the growth of tumors resulting from injection of Tax-deficient HTLV-I-infected cells in NOD/SCID $\beta 2m^{null}$ mice. Combined with previous studies, these results indicate that DHMEQ has strong potential for ATL therapy, regardless of whether Tax expression can be detected. In addition, our data provide a more extensive analysis of an NF-κB inhibitor predicted to act as an ATL chemotherapeutic agent in vivo than any other study to date.

Acknowledgements

References

[1] B.J. Poiesz, F.W. Ruscetti, A.F. Gazdar, P.A. Bunn, J.D. Minna, R.C. Gallo, Detection and isolation of type C retrovirus particles from fresh and cultured lymphocytes of a patient with cutaneous T cell lymphoma, Proc. Natl. Acad. Sci. USA 77 (1980) 7415–7419.

[2] Y. Hinuma, K. Nagata, M. Hanaoka, M. Nakai, T. Matsumoto, K.I. Kinoshita, et al., Adult T cell leukemia: antigen in an ATL cell line and detection of antibodies to the antigen in human sera, Proc. Natl. Acad. Sci. USA 78 (1981) 6476–6480.

[3] T. Watanabe, HTLV-I-associated diseases, Int. J. Hematol. 66 (1997) 257–278.

[4] Y. Yamada, M. Tomonaga, H. Fukuda, S. Hanada, A. Utsunomiya, M. Tara, et al., A new G-CSF-supported combination chemotherapy, LSG15, for adult T-cell leukaemia-lymphoma: Japan Clinical Oncology Group Study 9303, Br. J. Haematol. 113 (2001) 375–382.

[5] S. Yamaoka, G. Courtois, C. Bessia, S.T. Whiteside, R. Weil, F. Agou, et al., Complementation cloning of NEMO, a component of the IκB kinase complex essential for NF-κB activation, Cell 93 (1998) 1231–1240.

[6] S.C. Sun, S. Yamaoka, Activation of NF-kB by HTLV-I and implications for cell transformation, Oncogene 24 (2005) 5952–5964.

[7] N. Mori, M. Fujii, S. Ikeda, Y. Yamada, M. Tomonaga, D.W. Ballard, et al., Constitutive activation of NF-κB in primary adult T cell leukemia cells, Blood 93 (1999) 2360–2368.

[8] N. Hironaka, K. Mochida, N. Mori, M. Maeda, N. Yamamoto, S. Yamaoka, Tax-independent constitutive IκB kinase activation in adult T-cell leukemia cells, Neoplasia 6 (2004) 266–278.

[9] M. Watanabe, T. Ohsugi, M. Shoda, T. Ishida, S. Aizawa, M. Maruyama-Nagai, et al., Dual targeting of transformed and untransformed HTLV-1-infected T-cells by DHMEQ, a potent and selective inhibitor of NF-κB, as a strategy for chemoprevention and therapy of adult T cell leukemia, Blood 106 (2005) 2462–2471.

[10] R. Horie, T. Watanabe, K. Umezawa, Blocking NF-κB as a potential strategy to treat adult T-cell leukemia/lymphoma, Drug News Perspect. 19 (2006) 201–209.

[11] K. Umezawa, Inhibition of tumor growth by NF-κB inhibitors, Cancer Sci. 97 (2006) 990–995.

[12] N. Matsumoto, H. Iinuma, T. Sawa, T. Takeuchi, S. Hirano, T. Yoshioka, et al., Epoxyquinomicins A, B, C and D, new antibiotics from Amycolatopsis. II. Effect on type II collagen-induced arthritis in mice, J. Antibiot. (Tokyo) 50 (1997) 906–911.

[13] N. Matsumoto, A. Ariga, S. To-e, H. Nakamura, N. Agata, S. Hirano, et al., Synthesis of NF-κB activation inhibitors

derived from epoxyquinomicin C, Bioorg. Med. Chem. Lett. 10 (2000) 865–869.

[14] A. Ariga, J. Namekawa, N. Matsumoto, J. Inoue, K. Umezawa, Inhibition of tumor necrosis factor-α-induced nuclear translocation and activation of NF-κB by dehydroxymethylepoxyquinomicin, J. Biol. Chem. 277 (2002) 24625–24630.

[15] E. Kikuchi, Y. Horiguchi, J. Nakashima, K. Kuroda, M. Oya, T. Ohigashi, et al., Suppression of hormone-refractory prostate cancer by a novel nuclear factor κB inhibitor in nude mice, Cancer Res. 63 (2003) 107–110.

[16] D.V. Starenki, H. Namba, V.A. Saenko, A. Ohtsuru, S. Maeda, K. Umezawa, et al., Induction of thyroid cancer cell apoptosis by a novel nuclear factor κB inhibitor, dehydroxymethylepoxyquinomicin, Clin. Cancer Res. 10 (2004) 6821–6829.

[17] G. Matsumoto, M. Muta, K. Umezawa, T. Suzuki, K. Misumi, K. Tsuruta, et al., Enhancement of the caspase-independent apoptotic sensitivity of pancreatic cancer cells by DHMEQ, an NF-κB inhibitor, Int. J. Oncol. 27 (2005) 1247–1255.

[18] M. Watanabe, M.Z. Dewan, T. Okamura, M. Sasaki, K. Itoh, M. Higashihara, et al., A Novel NF-κB inhibitor DHMEQ selectively targets constitutive NF-κB activity and induces apoptosis of multiple myeloma cells in vitro and in vivo, Int. J. Cancer 114 (2005) 32–38.

[19] H. Tatetsu, Y. Okuno, M. Nakamura, F. Matsuno, T. Sonoki, I. Taniguchi, et al., Dehydroxymethylepoxyquinomicin, a novel nuclear factor-κB inhibitor, induces apoptosis in multiple myeloma cells in an IκBα-independent manner, Mol. Cancer Ther. 4 (2005) 1114–1120.

[20] G. Matsumoto, J. Namekawa, M. Muta, T. Nakamura, H. Bando, K. Tohyama, et al., Targeting of nuclear factor κB pathways by dehydroxymethylepoxyquinomicin, a novel inhibitor of breast carcinomas: antitumor and antiangiogenic potential in vivo, Clin. Cancer Res. 11 (2005) 1287–1293.

[21] T. Ohsugi, R. Horie, T. Kumasaka, A. Ishida, T. Ishida, K. Yamaguchi, et al., In vivo antitumor activity of the NF-kB inhibitor dehydroxymethylepoxyquinomicin in a mouse model of adult T-cell leukemia, Carcinogenesis 26 (2005) 1382–1388.

[22] T. Ohsugi, T. Kumasaka, A. Ishida, T. Ishida, R. Horie, T. Watanabe, et al., In vitro and in vivo antitumor activity of the NF-κB inhibitor DHMEQ in the human T-cell leukemia virus type I-infected cell line, HUT-102, Leukemia Res. 30 (2006) 90–97.

[23] S.W. Christianson, D.L. Greiner, R.A. Hesselton, J.H. Leif, E.J. Wagar, I.B. Schweitzer, et al., Enhanced human CD4+ T cell engraftment in β2-microglobulin-deficient NOD-scid mice, J. Immunol. 158 (1997) 3578–3586.

[24] K. Sugamura, M. Fujii, M. Kannagi, M. Sakitani, M. Takeuchi, Y. Hinuma, Cell surface phenotypes and expression of viral antigens of various human cell lines carrying human T-cell leukemia virus, Int. J. Cancer 34 (1984) 221–228.

[25] I. Miyoshi, I. Kubonishi, S. Yoshimoto, T. Akagi, Y. Ohtsuki, Y. Shiraishi, et al., Type C virus particles in a cord T-cell line derived by co-cultivating normal human cord leukocytes and human leukaemic T-cells, Nature 294 (1981) 770–771.

[26] T. Ohsugi, K. Kumasaka, T. Urano, Construction of a full-length human T cell leukemia virus type I (HTLV-I) genome from MT-2 cells containing multiple defective proviruses using overlapping polymerase chain reaction, Anal. Biochem. 329 (2004) 281–288.

[27] Y. Satou, K. Nosaka, Y. Koya, JI. Yasunaga, S. Toyokuni, M. Matsuoka, Proteasome inhibitor, bortezomib, potently inhibits the growth of adult T-cell leukemia cells both in vivo and in vitro, Leukemia 18 (2004) 1357–1363.

[28] T. Kinoshita, M. Shimoyama, K. Tobinai, M. Ito, S. Ito, S. Ikeda, et al., Detection of mRNA for the tax1/rex1 gene of human T-cell leukemia virus type I in fresh peripheral blood mononuclear cells of adult T-cell leukemia patients and viral carriers by using the polymerase chain reaction, Proc. Natl. Acad. Sci. USA 86 (1989) 5620–5624.

[29] Y. Furukawa, M. Osame, R. Kubota, M. Tara, M. Yoshida, Human T-cell leukemia virus type-1 (HTLV-1) Tax is expressed at the same level in infected cells of HTLV-1-associated myelopathy or tropical spastic paraparesis patients as in asymptomatic carriers but at a lower level in adult T-cell leukemia cells, Blood 85 (1995) 1865–1870.

Genome-Wide, High-Resolution Detection of Copy Number, Loss of Heterozygosity, and Genotypes from Formalin-Fixed, Paraffin-Embedded Tumor Tissue Using Microarrays

Sharoni Jacobs,[1] Ella R. Thompson,[2,3] Yasuhito Nannya,[4] Go Yamamoto,[4] Raji Pillai,[1] Seishi Ogawa,[5] Dione K. Bailey,[1] and Ian G. Campbell[2,3]

[1]Affymetrix, Inc., Santa Clara, California; [2]Victorian Breast Cancer Research Consortium Cancer Genetics Laboratory, Peter MacCallum Cancer Centre, East Melbourne, Victoria, Australia; [3]Department of Pathology, University of Melbourne, Parkville, Victoria, Australia; and Departments of [4]Hematology/Oncology and [5]Regeneration Medicine for Hematopoiesis, University of Tokyo, Tokyo, Japan

Abstract

Formalin-fixed, paraffin-embedded (FFPE) material tends to yield degraded DNA and is thus suboptimal for use in many downstream applications. We describe an integrated analysis of genotype, loss of heterozygosity (LOH), and copy number for DNA derived from FFPE tissues using oligonucleotide microarrays containing over 500K single nucleotide polymorphisms. A prequalifying PCR test predicted the performance of FFPE DNA on the microarrays better than age of FFPE sample. Although genotyping efficiency and reliability were reduced for FFPE DNA when compared with fresh samples, closer examination revealed methods to improve performance at the expense of variable reduction in resolution. Important steps were also identified that enable equivalent copy number and LOH profiles from paired FFPE and fresh frozen tumor samples. In conclusion, we have shown that the Mapping 500K arrays can be used with FFPE-derived samples to produce genotype, copy number, and LOH predictions, and we provide guidelines and suggestions for application of these samples to this integrated system. [Cancer Res 2007;67(6):2544-51]

Introduction

The challenges associated with DNA derived from formalin-fixed, paraffin-embedded (FFPE) samples have prevented widespread application of FFPE DNA to many of the technologies available for high-quality DNA, although some options with lower genomic coverage are available (1-3). In this study, we show the feasibility and limitations of a genome-wide assessment of genotype, loss of heterozygosity (LOH), and copy number using FFPE DNA on the Affymetrix Mapping 500K array set, which includes the Mapping 250K Nsp Array and the Mapping 250K Sty Array (Santa Clara, CA). These arrays use a process termed whole-genome sampling analysis (WGSA; ref. 4), in which genomic DNA is digested and ligated to adaptors. A subset of digested fragments are then PCR amplified in a complexity reduction step before hybridization to the arrays. PCR proved to be the critical step when processing FFPE samples.

We compared several extraction methods to determine which protocol provides FFPE DNA most suitable for array analysis and found that a PCR-based assessment of DNA quality predicted the downstream performance of FFPE DNA samples better than age of FFPE sample. We identified a necessity for (a) in silico compensation against fragment size bias and (b) a fragment size filter during analysis of FFPE samples. We tested our new guidelines for FFPE DNA qualification and analysis on archival samples of various tissue types, storage times, and location sources. Quality of FFPE DNA varied but the methods outlined by this study enabled prediction of performance. These results show that FFPE DNA can be suitable for a combined study of genotype, LOH, and copy number on a whole-genome scale.

Materials and Methods

Sample selection and DNA extraction. Five primary endometrioid ovarian cancers were selected without screening for the initial portion of this study. For each sample set, normal lymphocytic DNA, fresh tumor tissue, and FFPE tissue were analyzed. Samples were collected between 1993 and 1999 as part of a larger study of ovarian cancer in women living in and around Southampton, United Kingdom (5). At the time of collection, DNA was extracted from blood samples and fresh tumor biopsies were snap frozen in liquid nitrogen. A portion of each frozen tumor biopsy was sectioned to assess the proportion of tumor. For samples 526T and 594T, microdissection was done (6) to obtain DNA with a >80% tumor component. DNA was extracted from the fresh frozen tissue using a salt chloroform method (7).

In 2002, a portion of each frozen tumor biopsy was formalin fixed and paraffin embedded as described previously (8), with all tumors fixed in 10% neutral buffered formalin for <24 h at room temperature. At the time of DNA extraction, the FFPE tumors had been embedded in paraffin blocks for 3 years. Five sections (10 μm) were deparaffinized twice in xylene (5 min) and rehydrated in 100%, 90%, and 70% ethanol (1 min each). The sections were stained with hematoxylin (4 min) and washed with water (1 min), acid alcohol (10 s), water (1 min), Scott's tap water (1 min), and water (1 min). The sections were then stained with eosin (3 min), rinsed with water (10 s), and dehydrated in 70%, 90%, and 100% ethanol (30 s each). Tumor cells were manually microdissected under a dissecting microscope as described previously (6) to obtain high-purity (>80%) tumor DNA. The tumor component for sample 594 was high enough that it was not stained or microdissected. DNA was extracted from the five endometrioid FFPE tissues using a modified Qiagen protocol (Valencia, CA; described below). Following DNA extraction from FFPE tissue, a salt precipitation DNA cleanup was done as described in the Affymetrix GeneChip Mapping Assay Manuals.

For the study of independent sample sets, DNA was extracted from FFPE tissue from 17 breast tumors and 8 colorectal tumors. FFPE blocks were collected from 11 pathology laboratories and ranged in age from 1 to 17 years. The formalin fixation and paraffin embedding protocols used for these tissues are not known but are likely to be quite varied. For breast

tumors, 10 μm sections were deparaffinized, stained with H&E, and manually microdissected (described above). The colorectal tumors were not stained or microdissected due to their high tumor component. DNA was extracted from breast and colorectal tissues (described below), and as before, a salt precipitation DNA cleanup was done.

The collection and use of tissues for this study were approved by the appropriate institutional ethics committees.

Trial of DNA extraction methods for FFPE tissue. Five DNA extraction methods were trialed using whole 20 μm sections from three FFPE blocks. The methods that were compared were the MagneSil Genomic Fixed Tissue System (Promega,[6] Madison, WI), ChargeSwitch gDNA Micro Tissue kit (Invitrogen,[7] Carlsbad, CA), PureGene (Gentra Systems,[8] Minneapolis, MN), DNeasy Tissue kit (Qiagen[9]), and a phenol/chloroform extraction. With the exception of the DNeasy Tissue kit and phenol/chloroform, the extractions were done according to the manufacturer's instructions. The extractions done with the DNeasy Tissue kit and with phenol/chloroform both were modified to include an initial incubation at 95°C for 15 min followed by 5 min at room temperature as described previously (9), before being digested with proteinase K for 3 days at 56°C in a rotating oven with periodic mixing and fresh enzyme added each 24 h. A salt precipitation was done on DNA from all five extraction methods.

DNA quality assessment and preparation. The extracted DNA was quantified using UV spectroscopy at 260 nm. Random amplified polymorphic DNA-PCR (RAPD-PCR; ref. 10) was done to assess the quality of DNA and maximum fragment lengths as described previously using 50, 5, or 0.5 ng DNA (11). Qiagen HotStarTaq was used, with 0.4 units per reactions (Qiagen[9]). Products were visualized with ethidium bromide on a 3% gel.

Preparation and application of DNA to the mapping arrays. Matched fresh and FFPE samples were analyzed on the Affymetrix GeneChip Human Mapping 10K v2 Xba Array and 50K Xba Array and prepared using the Mapping 10K v2 Assay kit and the Mapping 100K Assay kit (Affymetrix)[10] The only exception to the manufacturer's protocol was that 10 cycles were added to the PCR cycling conditions for each FFPE sample.

Matched fresh tumor, FFPE tumor, and normal samples were assayed using the Mapping 250K Nsp Assay kit and the Mapping 250K Sty Assay kit[10] and hybridized to the 250K arrays. The 500K assay was done according to the manufacturer's protocol, beginning with 250 ng DNA. Ninety micrograms of PCR product were fragmented and labeled, using additional PCRs when necessary for FFPE breast and colorectal samples.

Data analysis. Genotype calls were produced using the dynamic model algorithm (12) by the Affymetrix GeneChip Genotyping Analysis Software version 4.0. A stringent P value cutoff threshold of 0.26 was used. Concordance was determined by calculating the number of single nucleotide polymorphisms (SNP) that gave the same call in both fresh frozen and FFPE DNA from the same tumor and dividing this number by the total number of SNPs that were called in both samples.

LOH predictions were produced using dChipSNP software (dChip2005_f4 version[11]; ref. 13). LOH values were inferred using the Hidden Markov Model and restricting to SNPs on fragment sizes ≤700 bp.

Copy number estimates for ovarian tumor samples using 500K data were determined by pairing tumor and matching normal samples in CNAG_v2.0.[12] Nonpaired, nonmatching references were used for copy number prediction of 10K and 50K data. Log 2 ratios were imported into Spotfire DecisionSite (Spotfire,[13] Somerville, MA) and the Affymetrix Integrated Genome Browser for visualization and comparison. Copy number estimates for breast and colon FFPE tumors were done using data from 48 HapMap samples (available online[10]) as a reference.

[6] http://www.promega.com
[7] http://www.invitrogen.com
[8] http://www.gentra.com
[9] http://www.qiagen.com
[10] http://www.affymetrix.com
[11] http://www.dchip.org
[12] http://www.genome.umin.jp/
[13] http://www.spotfire.com

Estimated inter-SNP mean and median distances after exclusion of fragment sizes >700 bp were determined by first calculating the distance between all SNPs on each chromosome. Distances were then sorted per chromosome in descending order and the largest distances (representing centromeres) were removed for each chromosome, except for the acrocentric chromosomes 13 to 15 and 21 to 22.

Pearson (linear) correlations were calculated in Partek Genomics Suite (Partek,[14] St. Louis, MO).

Microsatellite analysis. Nine microsatellite markers were used to assess LOH at three loci: chromosome 1q (D1S2816, D1S413, and D1S1726), chromosome 7p (D7S691, D7S670, and D7S2506), and chromosome 14q (D14S1011, D14S258, and D14S1002). Regions were selected where array-based LOH analysis showed discordant LOH results for fresh and FFPE-derived DNA. The forward primer was labeled with a 5'-fluorescent dye (FAM or HEX). The samples were analyzed using a 3130 Genetic Analyzer (Applied Biosystems,[15] Foster City, CA) with POP7 polymer. An assessment of LOH was done using GeneMapper version 3.7. LOH was scored by calculation of the ratio of tumor DNA peaks (T1/T2) compared with that in the normal DNA to give a relative ratio (T1/T2)/(N1/N2). A ratio of 0 indicates complete allele loss and a ratio of 1 indicates no LOH. A ratio of ≤0.5 was scored as indicative of LOH.

Results

DNA extraction from FFPE tissue. Five DNA extraction methods (phenol/chloroform, Qiagen DNeasy Tissue kit, Invitrogen ChargeSwitch, Promega MagneSil, and Gentra PureGene) were tested on consecutive sections from different FFPE ovarian tumor biopsies. Phenol/chloroform and modified Qiagen protocols (see Materials and Methods) provided the highest DNA yield as determined by UV spectroscopy; these yields were 2.2 times more than the average yield from any of the other three extraction protocols (Fig. 1A). RAPD-PCR, which uses primers of 10 bps to produce a ladder of amplicons, was also done to assess both amplification efficiency and maximum product size for each extraction protocol (11). Compared with DNA extracted from fresh lymphocytes, the FFPE-derived DNA from all extraction methods yielded consistently smaller PCR fragments, with a maximum reliable size of ~800 bp (Fig. 1A). Phenol/chloroform and modified Qiagen extractions produced more intense and consistent PCR fragments across dilutions, suggesting that products were relatively free of contaminant inhibitors (Fig. 1A). DNA extracted with these two methods was processed through the PCR step of the Mapping 50K Xba Assay to further assess amplification efficiency. In this test, the modified Qiagen extraction provided a slightly higher PCR yield on average than the phenol/chloroform method (21.4 μg compared with 19.2 μg) and was therefore chosen for DNA extraction from FFPE tissues in this study.

Mapping 500K array performance. Five matched sets; each containing (a) nontumor, non-FFPE lymphocytic DNA, (b) fresh frozen ovarian tumor DNA, and (c) FFPE ovarian tumor DNA; were assessed for performance on the Mapping 500K arrays. All five FFPE samples had been stored for 3 years and provided average RAPD-PCR maximum amplicon sizes from 526 to 800 bp. During the PCR step of the Mapping assay, amplification products from all five FFPE tumors were concentrated <700 bp, a fragment size range that was reduced compared with non-FFPE samples (Fig. 1B). Decreased yield from the Mapping PCRs (Table 1) accompanied the decrease in amplicon size distributions. FFPE samples produced

[14] http://www.partek.com
[15] http://www.appliedbiosystems.com

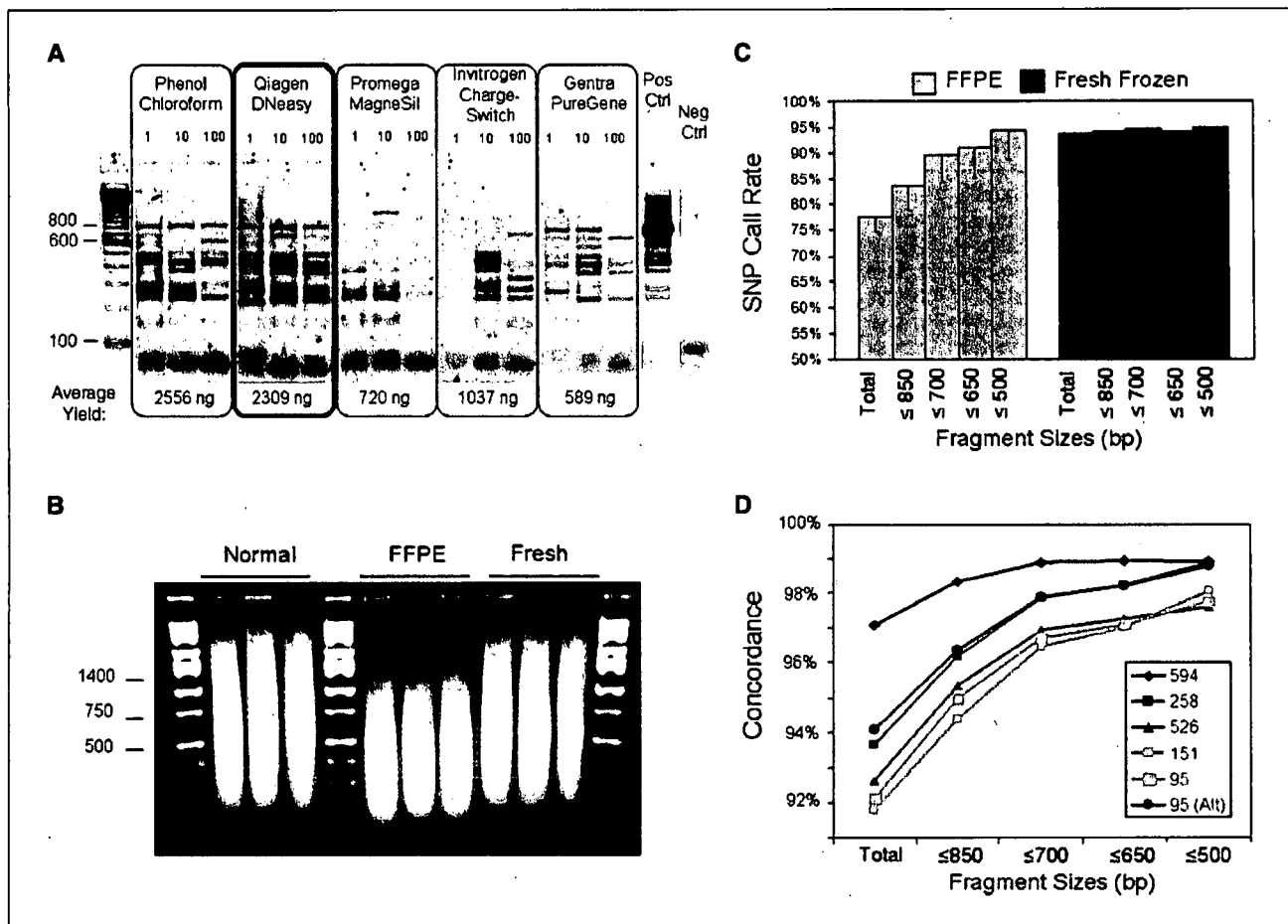**Figure 1.** Performance of different FFPE DNA extraction methods and the Affymetrix GeneChip Mapping 500K assay. A, visualization of RAPD-PCR products on a 3% agarose gel comparing the undiluted DNA extraction (1), a 1:10 dilution of input DNA (10), and a 1:100 dilution of DNA (100) from one FFPE tissue (047) using five different extraction methods. The maximum fragment size in the extracted FFPE DNA samples reached 1,100 bp although only with sample dilution. The maximum reproducible fragment was 800 bp. DNA yield per extraction method is listed below. B, visualization of the PCR products during the Mapping 500K assay reveals a downshift in the distribution of fragment size, which is specific to the FFPE samples. C, SNP call rates are reduced in FFPE samples, but SNPs on smaller fragments are genotyped with equal efficiency from fresh and paraffin samples. The size dependence for higher call rates is specific to the FFPE samples. D, concordance between fresh frozen and matching FFPE samples is incrementally increased with fragment size selectivity, with larger dips in accuracy for sizes >700 bp. Exclusion of some regions (chromosomes 1q, 7p, 15, and 16q) shown to be genetically different between 95 fresh and FFPE samples causes an upshift in concordance for this sample (95 Alt versus 95).

63 to 83 μg PCR products for the Mapping 250K Nsp Array, whereas all non-FFPE samples produced >90 μg.

The assay was continued using 90 μg PCR product as the manual instructs or the total PCR yield when this was less than assay requirements. Importantly, the protocol was otherwise never modified. Normal and fresh tumor samples gave typical SNP call rates, with an average of 94.5% and 93.5%, respectively. These call rates are lowered due to application of a strict confidence score threshold ($P \leq 0.26$; the default threshold is $P \leq 0.33$). In contrast, FFPE samples achieved an overall average call rate of 79.84% and 75.17% for Nsp and Sty, respectively (Table 1). These decreased call rates are consistent with the poor amplification of larger fragments during PCR. Exclusion of SNPs on larger fragments significantly increased the call rates, such that incrementally more stringent fragment size restrictions incrementally increased call rates (Fig. 1C). In fact, stringent fragment size restrictions produced similar call rates between fresh frozen and FFPE samples, indicating that the Mapping 500K is well suited for FFPE DNA

and identifying the limiting factor as the size of amplicons produced from the degraded DNA.

Concordance of genotype calls between paired FFPE and fresh frozen ovarian tumor DNA samples was examined to determine the reliability of genotypes from FFPE DNA. It is important to note that tumor heterogeneity lead to confirmed genuine differences in genomic content between matched FFPE and fresh frozen DNA, which would lower these concordance rates. Average overall concordance between FFPE and fresh frozen samples from the same tumor was 93.6%. Exclusion of the larger fragments increased concordance such that all SNPs located on fragment sizes ≤700 bp displayed an average of 97.4% concordance (Fig. 1D). Exclusion of several regions (chromosomes 1q, 7p, 15, and 16q) displaying heterogeneity between fresh frozen and paraffin sample 95 increased the concordance by >2% (Fig. 1D). These high rates of concordance, despite shown genetic differences between paired samples, underscore the reliability and reproducibility of genotype calls produced using FFPE-derived DNA samples with this

Table 1. Performance of normal, fresh frozen, and FFPE samples on Affymetrix GeneChip Mapping 10K v2, 50K Xba, 250K Nsp, and 250K Sty arrays

Type	Array	PCR yield* (μg)	Call rate[†] (%)	AA call (%)	AB call (%)	BB call (%)	Signal detection[‡] (%)	MCR[§] (%)	MDR[ǁ] (%)	Overall concordance[¶] (%)
Fresh tumor	10K v2	20.4	93.44	37.96	23.50	38.54	99.82	—	—	96.20
FFPE tumor	10K v2	19.2	86.30	39.77	19.83	40.41	97.39	—	—	
Fresh tumor	50K Xba	48.3	90.07	40.28	20.24	39.48	—	87.65	98.57	56.95
FFPE tumor	50K Xba	46.0	31.86	47.30	6.76	45.94	—	15.25	22.15	
Normal	250K Nsp	115.1	95.86	37.95	25.54	36.51	—	94.22	98.60	
Fresh tumor	250K Nsp	114.4	93.99	41.81	18.09	40.10	—	88.26	98.52	94.74
FFPE tumor	250K Nsp	71.6	79.84	43.42	14.89	41.69	—	65.60	80.32	
Normal	250K Sty	121.1	93.05	38.87	24.28	36.85	—	90.90	97.45	
Fresh tumor	250K Sty	114.4	92.96	42.38	17.59	40.03	—	87.95	98.38	92.07
FFPE tumor	250K Sty	95.4	75.17	43.66	16.68	39.66	—	62.57	79.37	

*For the 250K arrays, this is the total yield of DNA obtained after combining three PCRs according to protocol. For the 10K v2 and 50K arrays, the PCR yield for the FFPE tissues was increased by increasing either the number of reactions or the number of PCR cycles.
[†] Percentage of SNPs able to be genotyped.
[‡] Signal detection used to assess 10K arrays.
[§] Modified partitioning around medoids (MPAM; a genotyping algorithm; ref. 17) call rate used to assess 100K and 500K arrays.
[ǁ] MPAM detection rate used to assess 100K and 500K arrays.
[¶] Percentage of SNPs genotyped in both fresh frozen and FFPE samples that are given the same genotype.

platform. Importantly, it indicates the need to exclude SNPs on larger fragments for reliable genotype data. Because SNP fragment size is distributed randomly across the genome, the general effect of excluding larger fragment sizes is to reduce the overall resolution without preferentially losing extensive coverage in specific regions (see Supplementary Fig. S1). The effect of fragment size on concordance was specific to FFPE samples and is not observed in comparisons between frozen samples (data not shown).

LOH and copy number assessment. The reliability of genotype assignments using paraffin samples suggests their suitability for LOH predictions. In fact, FFPE and fresh tumor pairs produced similar LOH profiles when including SNPs on fragments sizes ≤700 bp (Fig. 2A). Regions of inconsistent LOH predictions between paired samples (for example, see Fig. 2A, boxes) were predicted independently by both Nsp and Sty arrays and appeared along concentrated regions, rather than being sporadically distributed across the genome, suggesting that they reflected true biological differences between the samples. We assessed several discordant regions of LOH using conventional microsatellite marker analysis and in all cases, the microsatellite analysis confirmed that the array predictions were genuine (data not shown).

The ability to associate copy number estimates with SNP genotypes relies on quantitation of SNP probe intensities (14). Because larger fragment SNPs were inadequately amplified during WGSA, these SNPs were noninformative for copy number analysis of FFPE samples (Supplementary Fig. S2A). Exclusion of these large fragment SNPs significantly increased the amplitude (signal) of copy number shifts and at the same time reduced the SD (noise) associated with the copy number estimates for all FFPE samples but not the fresh frozen samples (Supplementary Fig. S2B). This increase in signal to noise ratio justifies the use of such a filter, which maintained 308,788 SNPs for FFPE copy number analysis (Table 2). Probe intensities from the remaining smaller fragment SNPs predicted copy number profiles for FFPE samples consistent with those from matching fresh frozen material (Fig. 2B).

Equivalent copy number changes were predicted between FFPE and fresh frozen pairs both across different chromosomes and different sample sets (Fig. 2C).

In addition to limiting fragment size, compensation against fragment size bias was necessary to produce reliable copy number predictions. Although bias due to amplicon size can be negligible when using high-quality DNA, it becomes exaggerated when the DNA sample is degraded (Fig. 3, top). For FFPE samples, the mean copy number was grossly affected by the size of the amplicon carrying the SNP, such that smaller amplicons SNPs predicted gains and larger amplicons SNPs predicted losses in copy number. Quadratic regression helped to neutralize this fluctuation in mean copy number (Fig. 3, middle). Exclusion of SNPs on amplicons >700 bp before regression effectively removed the fragment size bias from copy number detection (Fig. 3, bottom). Copy number analysis of FFPE samples was done using the freely available CNAG_v2.0 software[12] (15), which automatically uses compensation against fragment size bias and includes an option to exclude SNPs based on fragment size. Alternate software tools that lack this compensation produced copy number estimates from FFPE samples that were noisier even with exclusion of large fragment sizes (data not shown).

Comparison of Mapping 10K, 100K, and 500K array performance. Although the various Mapping arrays all use the same technology and similar assays for genotype and copy number analysis, they each have differences that may influence their compatibility with FFPE samples. Particularly, the Mapping 500K and 10K arrays share the same amplicon distribution during the PCR step of WGSA, but the Mapping 100K assay relies on a wider amplicon size distribution (250–2,000 bp). Consequently, Mapping 100K data are more significantly affected by DNA degradation; for example, there are only 59 SNPs on fragment sizes <500 bp on the Mapping 50K Hind array. Previously, we showed the application of FFPE DNA to the 10K arrays (3) although without the analytic tools applied here. Now, we compared performance of FFPE samples on all Mapping arrays. As expected, call rates and concordances were

poor when FFPE DNA was applied to the Mapping 100K assay, whereas performance was similar for the Mapping 500K and 10K arrays (Table 1; Supplementary Fig. S3). Furthermore, both the Mapping 500K and the 10K arrays, but not the Mapping 100K arrays, provided correct copy number predictions from FFPE DNA, whereas the Mapping 500K arrays best accommodated SNP filters to retain high genomic resolution (Supplementary Fig. S3).

Prediction of mapping array performance for a range of FFPE samples. DNA from FFPE samples can vary in quality as a result of the fixation protocol, years of storage, the extraction protocol, tissue source, and several other uncontrollable and controllable variables. To both identify a method for qualifying FFPE DNA samples for array analysis and test our guidelines for FFPE DNA extraction and data analysis, we measured the performance of an additional 25 FFPE tissue sources processed at separate institutes and stored for 1 to 17 years (Supplementary Table S1). These samples were not prescreened nor selected based on expected performance. Experiments were done without

matched fresh frozen or nontumor samples. In a small test set, we found that application of 90 μg PCR product from FFPE samples increased call rates by several percentage points (data not shown); therefore, we assayed these samples using 90 μg whenever possible, even if this required pooling extra PCRs.

For each sample, we noted the largest amplicon size produced during RAPD-PCR as well as the size range of PCR products during the Mapping assay. Call rates were calculated for SNPs on fragment size ≤200 bp, 250 bp, 300 bp, and so on to determine the size at which call rates dropped <90%. This call rate drop-off value was used to indicate genotyping efficiency and reliability because fragment sizes with high call rates provided high concordance as well. Call rate drop-off values ranged from 250 to 750 bp compared with 700 to 850 bp for the five FFPE ovarian tumors. Therefore, most of these samples would provide reduced resolution for genotype and LOH. Copy number detection was more robust than genotype, and those cutoffs ranged from 300 bp up to no filter requirement at all. Plots of copy number versus fragment size were evaluated to
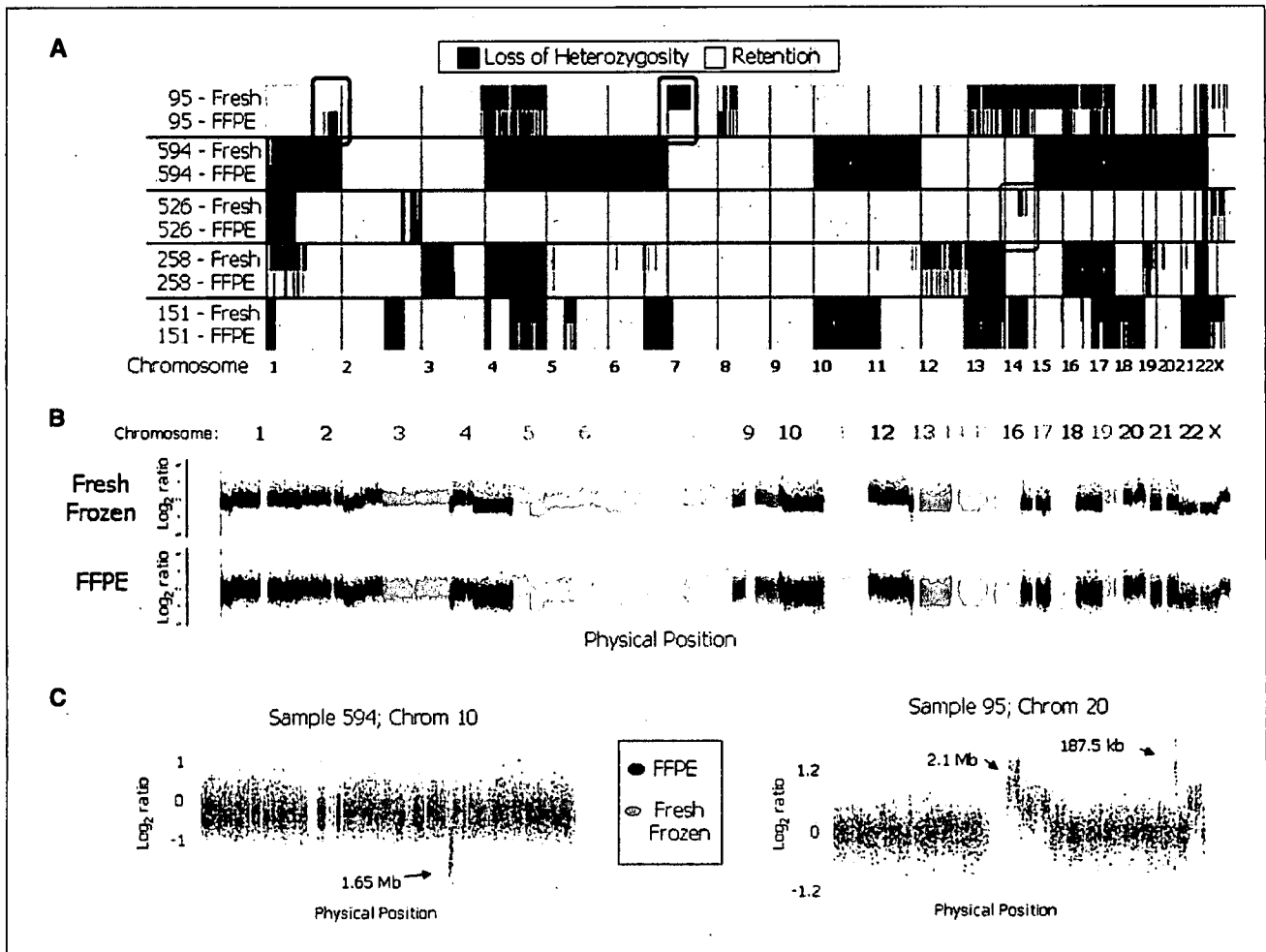

Figure 2. Genome-wide plots of LOH and copy number for fresh frozen and FFPE samples. *A,* genome-wide display of inferred LOH for fresh frozen and FFPE samples, including SNPs on fragments sizes ≤700 bp. *Blue regions,* LOH; *yellow regions,* retention of heterozygosity. Chromosome numbers are indicated below. Three discordant LOH predictions specific to either fresh frozen or FFPE samples were confirmed by microsatellite analysis of DNA (*brown boxes,* regions). *B,* raw single SNP log 2 ratios indicate gains and losses for fresh frozen (above) and FFPE (below) sources of sample 151 across the genome. Ratios represent copy number of tumor DNA over copy number of nontumor, non-FFPE lymphocytic DNA. Each color represents a different chromosome. SNPs were filtered for fragments ≤700 bp for the FFPE sample. *C,* raw single SNP log 2 ratios for fresh frozen (*orange*) and FFPE (*blue*) DNA are plotted across single chromosomes of multiple samples. SNPs were filtered for fragments ≤700 bp for FFPE data only. Highlighted copy number changes were confirmed by quantitative PCR.

Table 2. SNP numbers per fragment size filters

Fragment sizes included (bp)	250K Nsp array	250K Sty array	500K array set
≤300	13,636	15,845	29,481
≤400	39,492	45,473	84,965
≤500	74,372	82,099	156,471
≤600	113,687	120,025	233,712
≤650	133,748	138,282	272,030
≤700	153,198	155,590	308,788
≤800	190,899	187,687	378,586
≤850	209,017	201,004	410,021
≤900	222,316	213,300	435,616
≤1,000	244,644	230,527	475,171
Total	262,256	238,300	500,568

determine the optimal fragment size filter for copy number analysis. These plots can be viewed in CNAG_v2.0, and various fragment size filters can be applied until the mean copy number for the SNPs retained in analysis are consistent across fragment size (Fig. 4C, left). An example of this entire workflow is shown in Fig. 4A to C and results are listed in Supplementary Table S1. As shown for a 733-kb hemizygous loss highlighted in this example, the fragment size filter suggested by this process was able to increase the signal to noise ratio by preferentially removing the noisy SNPs instead of the informative SNPs and at the same time was also able to retain higher resolution by not overfiltering (Fig. 4C, right).

Years of storage and overall call rates displayed some correlation to copy number and call rate drop-off values, but PCR-based analyses had higher predictive power for these performance metrics (Fig. 4D). The Pearson's correlation of median RAPD-PCR values to copy number drop-off was 0.93, indicating high predictive power. Comparison of array performance to PCR-based DNA quality tests gave R^2 values above 0.8. In contrast, R^2 values were <0.7 when comparing performance with years of storage or comparing copy number drop-off with overall call rate. These results indicate that a PCR-based test of DNA quality is a reasonable method for predicting whether a FFPE DNA sample will be amenable to array analysis.

Six of the 25 samples (two breast and four colorectal) were not applied to the arrays because no RAPD-PCR products were produced. Sample 0588 also failed RAPD-PCR, but it was still applied to the array. Consistent with the RAPD-PCR prediction, this sample was the only example, in which call rates broken up by fragment size never exceeded 90%, and data from even the smallest fragment SNPs were too noisy for copy number analysis.

Discussion

There exists a large and growing deposit of archived clinical tissues, yet DNA extracted from these samples is usually degraded, contaminated, and of general low quality. This study expands the usefulness of the Mapping 500K arrays to DNA derived from FFPE samples, showing that the limiting factor for FFPE application is the size distribution of PCR amplicons during WGSA. The maximum amplifiable fragment size, which is correlated to array performance, varied between samples and may be influenced by

Figure 3. Compensation against fragment size bias enables effective copy number analysis of FFPE samples. Raw predicted copy number (*Y-axes*) is influenced by fragment size (*X-axes*) in fresh frozen (*right*) and FFPE (*left*) samples, although the effect is exaggerated in the latter (see *blue solid lines, middle*). This causes an overestimate of copy number for fragments below ~500 bp and an underestimate for those above ~500 bp. Compensation against fragment size corrects this bias such that the mean predicted copy number (*blue line*) is constant independent of fragment size in fresh frozen samples (*bottom right*). For FFPE samples, exclusion of noninformative larger fragments before quadratic regression is required to effectively equilibrate copy number across maintained SNPs (*top left*).
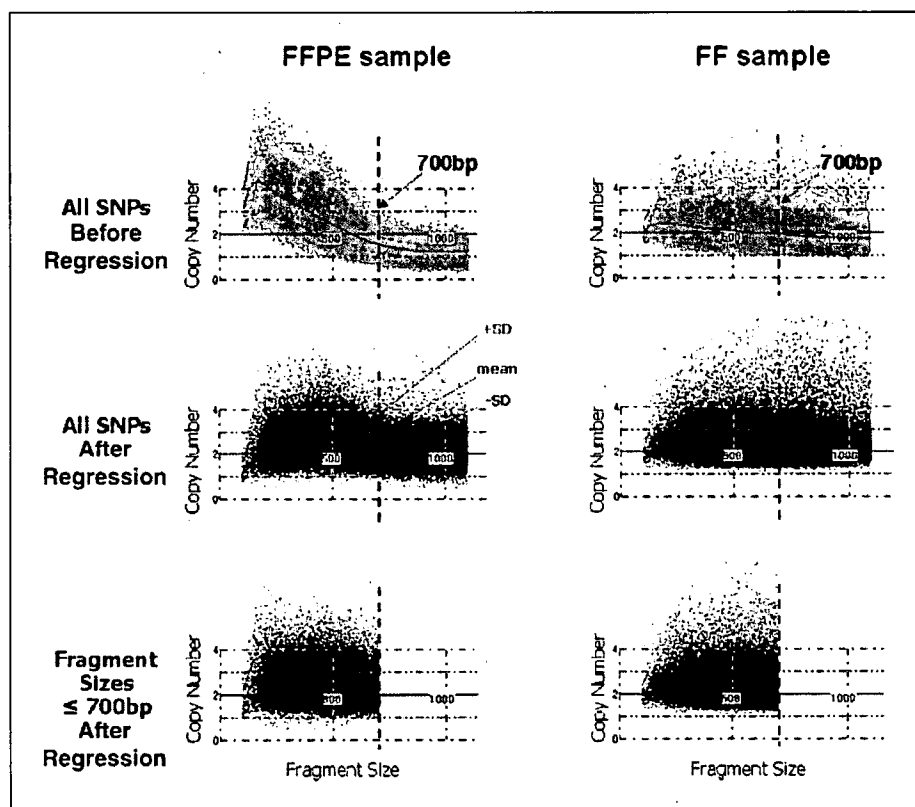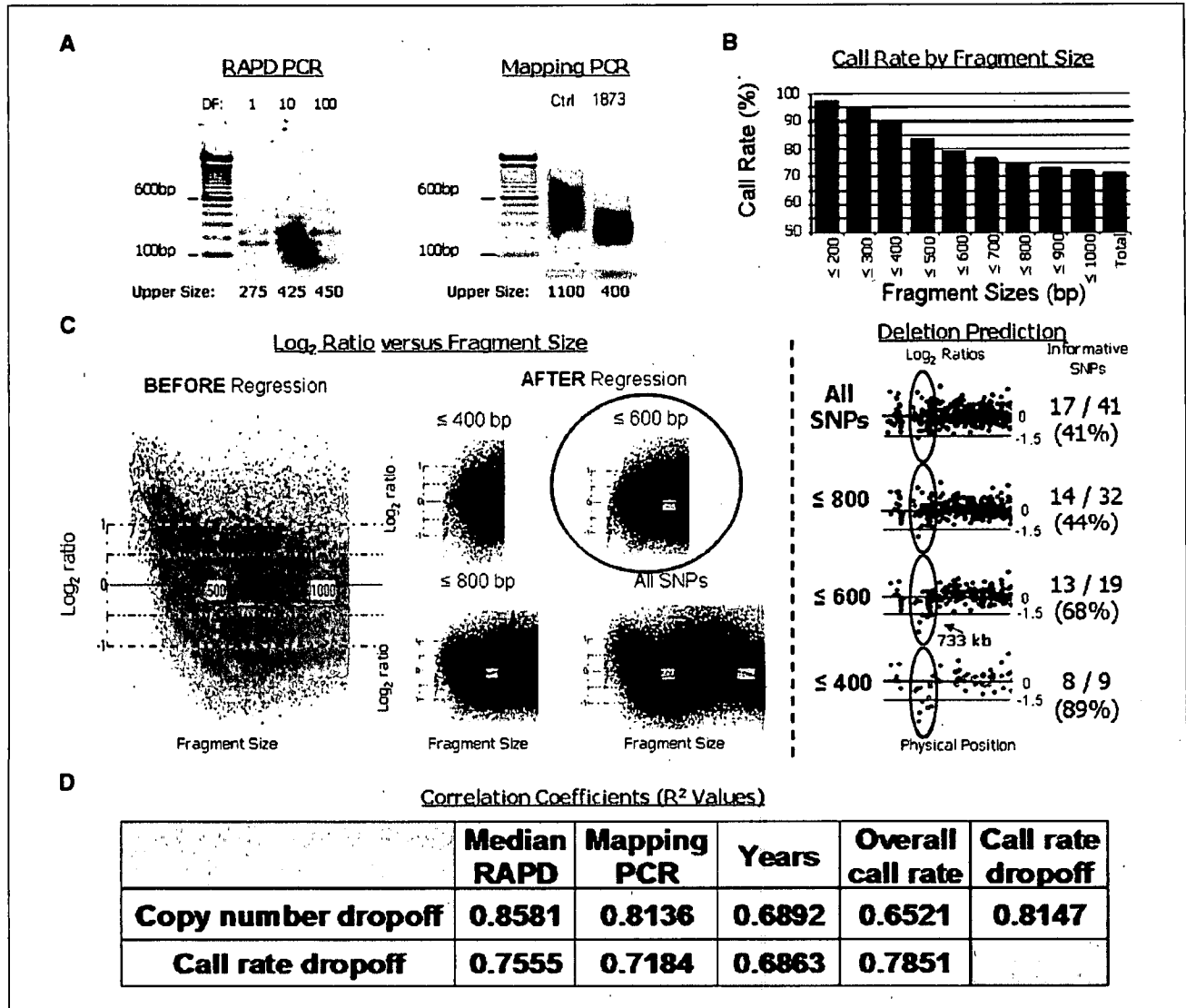
Figure 4. Prediction of FFPE sample performance. A, display of RAPD-PCR and Mapping assay PCR for a single breast tumor sample (1873). Maximum size amplicons from RAPD-PCR varied from 275 to 450 bp, with dilution factors (DF) of 1, 10, and 100. Although high-quality DNA had a maximum upper fragment size of ~1,100 after PCR during the Mapping assay, this sample was well amplified only up to ~400 bp. B, call rate by fragment size was monitored for the same sample, using a stringent confidence value threshold of 0.26. Call rates dropped <90% when excluding SNPs on fragment sizes >400 bp. C, copy number versus fragment size plots in CNAG_v2.0 show a strong influence by fragment size on copy number predictions before correction (left). Regression corrects this bias somewhat, and more and more stringent filters further correct this bias (middle). With a filter excluding SNPs on fragment sizes >600 bp, the mean copy number (blue line) is consistent regardless of fragment size, indicating that this sample requires a copy number filter at 600 bp. Log 2 ratios produced using various fragment size filters are displayed for a region containing a 733-kb deletion on part of chromosome X. Under "Informative SNPs," the number of SNPs predicting a deletion with a log 2 ratio below −0.3 (considered to be "informative") are listed to the left of the number of total SNPs within the deletion region that were retained during the fragment size filter. Below these values is the percentage of SNPs included in the analysis that were informative of the deletion. D, R^2 regression values when the fragment size at which call rates drop <90% or the maximum fragment size that can be included in copy number analyses are compared with median maximum RAPD-PCR amplicon size, maximum Mapping PCR amplicon size, years of storage, or overall call rate ($P \leq 0.26$) are displayed. PCR tests better predicted copy number performance than years of storage or overall call rate, and they were better predictors of genotype performance than years of storage was.

both extent of DNA degradation and modification as well as the amount of inhibitors remaining in the sample. Use of a suitable DNA extraction protocol, such as the DNeasy Tissue kit, is important for obtaining DNA amenable to the assay, but other factors, such as years of storage and fixation process, will be harder to control. This underscores the necessity for a pre-WGSA quality control step that includes PCR of larger fragment sizes, such as RAPD-PCR or multiplex PCR (16). This study attempts to outline guidelines for qualifying FFPE DNA samples and analyzing qualified samples, but not all FFPE blocks will yield DNA suitable for the Mapping arrays.

FFPE DNA that is applied to the arrays may still vary in quality and therefore require more or less stringent fragment size filters. Despite reduction in coverage to accommodate loss of larger fragments, high resolution for genotype, LOH, and copy number assessment can still be maintained (Table 2; Supplementary Fig. S1). This is true because of the large number of SNPs on small fragments and because fragment size seems to be the only limiting

factor. For example, with exclusion of SNPs on amplicons >700 bp, as was required for the first set of five FFPE samples, 308,788 SNPs were retained for analysis, providing a median and mean inter-SNP distance of 4.3 or 9.5 kb, respectively. Although the 10K array is also suitable for analysis of degraded DNA (3), the large SNP coverage and the small fragment emphasis of the Mapping 500K arrays make it ideal for FFPE sample analysis.

The percentage of FFPE samples archived in banks that could be applied to the arrays with limited loss in genomic resolution would be influenced by the methods of fixation and extraction used at various institutes. Importantly, all samples stored for 6 years or fewer provided copy number data for a minimum of 234K SNPs in this study. Some of the samples applied to the arrays required extremely stringent filters against fragment size, resulting in significantly decreased resolution of genomic data. Potentially, researchers may choose only to analyze DNA samples of such low quality when the FFPE sample is considered to be particularly precious. Importantly, RAPD-PCR results predicted that these samples would display decreased performance on the array and a PCR screen could be applied to avoid application of poorly doing samples. With the advent of more standardized protocols for sample processing in the future and with advances in DNA extraction, a higher proportion of FFPE samples may be applicable to the arrays.

Despite the large banks of FFPE samples available for retrospective studies that include follow-up analysis of patient outcome, most of these studies currently focus on frozen samples because of the limited options available for paraffin samples. Additionally, FFPE processing holds advantages for tissue storage during prospective studies, in which many biopsies are collected but only a fraction of them are applied to downstream assays with selection based on clinical outcome. These results outline guidelines for the application of FFPE samples to the same genome-wide platform already available to high-quality DNA samples, thus enabling widespread retrospective and prospective analysis of tumor samples in their most common form of storage.

Acknowledgments

References

1. Wang Y, Moorhead M, Karlin-Neumann G, et al. Allele quantification using molecular inversion probes (MIP). Nucleic Acids Res 2005;33:e183.
2. Lips EH, Dierssen JW, van Eijk R, et al. Reliable high-throughput genotyping and loss-of-heterozygosity detection in formalin-fixed, paraffin-embedded tumors using single nucleotide polymorphism arrays. Cancer Res 2005;65:10188–91.
3. Thompson ER, Herbert SC, Forrest SM, Campbell IG. Whole genome SNP arrays using DNA derived from formalin-fixed, paraffin-embedded ovarian tumor tissue. Hum Mutat 2005;26:384–9.
4. Kennedy GC, Matsuzaki H, Dong S, et al. Large-scale genotyping of complex DNA. Nat Biotechnol 2003;21: 1233–7.
5. Bryan EJ, Watson RH, Davis M, Hitchcock A, Foulkes WD, Campbell IG. Localization of an ovarian cancer tumor suppressor gene to a 0.5-cM region between D22S284 and CYP2D, on chromosome 22q. Cancer Res 1996;56:719–21.

6. Jiang X, Hitchcock A, Bryan EJ, et al. Microsatellite analysis of endometriosis reveals loss of heterozygosity at candidate ovarian tumor suppressor gene loci. Cancer Res 1996;56:3534–9.
7. Mullenbach R, Lagoda PJL, Welter C. An efficient salt chloroform extraction of DNA from blood and tissues. Trends Genet 1989;5:391.
8. Bancroft JD, Stevens A. Theory and practice of histological techniques. 3rd ed. London: Churchill Livingstone; 1991. p. 48–57.
9. Wu L, Patten N, Yamashiro CT, Chui B. Extraction and amplification of DNA from formalin-fixed, paraffin-embedded tissues. Appl Immunohistochem Mol Morphol 2002;10:269–74.
10. Williams JG, Kubelik AR, Livak KJ, Rafalski JA, Tingey SV. DNA polymorphisms amplified by arbitrary primers are useful as genetic markers. Nucleic Acids Res 1990;18: 6531–5.
11. Siwoski A, Ishkanian A, Garnis C, Zhang L, Rosin M, Lam WL. An efficient method for the assessment of DNA quality of archival microdissected specimens. Mod Pathol 2002;15:889–92.

12. Di X, Matsuzaki H, Webster TA, et al. Dynamic model based algorithms for screening and genotyping over 100 K SNPs on oligonucleotide microarrays. Bioinformatics 2005;21:1958–63.
13. Lin M, Wei LJ, Sellers WR, Lieberfarb M, Wong WH, Li C. dChipSNP: significance curve and clustering of SNP-array-based loss-of-heterozygosity data. Bioinformatics 2004;20:1233–40.
14. Huang J, Wei W, Zhang J, et al. Whole genome DNA copy number changes identified by high density oligonucleotide arrays. Hum Genomics 2004; 1:287–99.
15. Nannya Y, Sanada M, Nakazaki K, et al. A robust algorithm for copy number detection using high-density oligonucleotide single nucleotide polymorphism genotyping arrays. Cancer Res 2005;65:6071–9.
16. van Beers EH, Joosse SA, Ligtenberg MJ, et al. A multiplex PCR predictor for aCGH success of FFPE samples. Br J Cancer 2006;94:333–7.
17. Liu WM, Di X, Yang G, et al. Algorithms for large-scale genotyping microarrays. Bioinformatics 2003;19: 2397–403.